論文 / 著書情報
Article / Book Information

題目(和文)	LiCoO2/Li10GeP2S12 ならびにTiS2/Li10GeP2S12 複合体電極の作製と全固体電池特性
Title(English)	Fabrication and electrochemical properties of LiCoO2/Li10GeP2S12 and TiS2/Li10GeP2S12 composite electrodes for all solid-state batteries
著者(和文)	LIWEN JING
Author(English)	Wen Jing Li
出典(和文)	学位:博士（工学）, 学位授与機関:東京工業大学, 報告番号:甲第10193号, 授与年月日:2016年3月26日, 学位の種別:課程博士, 審査員:菅野 了次,平山 雅章,大坂 武男,北村 房男　,中村 二朗
Citation(English)	Degree:, Conferring organization: Tokyo Institute of Technology, Report number:甲第10193号, Conferred date:2016/3/26, Degree Type:Course doctor, Examiner:,,,,
学位種別(和文)	博士論文
Type(English)	Doctoral Thesis

Fabrication and electrochemical properties of $LiCoO_2/Li_{10}GeP_2S_{12}$ and $TiS_2/Li_{10}GeP_2S_{12}$ composite electrodes for all solid-state batteries

Li Wen Jing

Department of Electronic Chemistry

Interdisciplinary Graduate School of Science and Engineering

Tokyo Institute of Technology

Contents

Chapter 1

Introduction

1.1 History of lithium battery

The first rechargeable lithium battery using an intercalation compound was demonstrated by Whittingam in 1976 [1, 2]. The battery consisted of a layered chalcogenide TiS_2 as the cathode, Li metal or Li-Al alloys as the anode, and lithium perchlorate in dioxolane as the electrolyte. Lithium has the most negative electrochemical potential of -3.04 V *vs.* SHE and the lowest volume density of 0.53 g cm^{-3}, which leading to high energy density of batteries. Thus, the lithium metal batteries were much attracted in 1970's. However, dendrite of lithium metal formed during charge-discharge operation may lead to explosion of the batteries shown in Figure 1a, which is the critical disadvantage. To solve the safety problem, the concept of rocking-chair type batteries using lithium intercalation materials was demonstrated, which are so-called lithium-ion batteries [3-6]. As shown in Figure 1b, lithium ions deintercalate from an anode material and intercalate into a cathode material at discharging, and the reactions reversibly proceed at charging. As lithium metal does not participate the battery reaction, the growth of the lithium dendrites can be suppressed. In 1980s, layered rocksalt-type Li*M*O_2 (*M*= Co, Ni, Mn) [7, 8] and carbonaceous materials [9, 10] were discovered as intercalation cathodes and anodes, respectively. Following these groundbreaking researches, the first commercial lithium-ion batteries was introduced by Sony in 1990, and the successful rechargeable lithium battery represented a revolution in the power source industry [12-14].

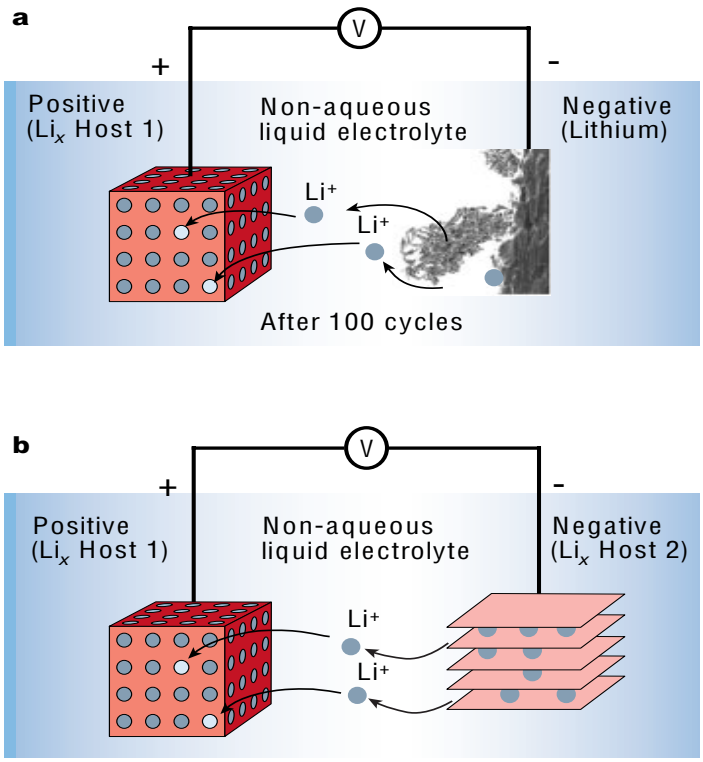

Figure 1. Schematic representation and operating principles of (a) Li-metal batteries and (b) Li-ion batteries [11].

The electrochemical reactions in lithium-ion batteries with the $LiCoO_2$ cathode and the graphite anode are expressed as follows.

Cathode: $LiCoO_2 \leftrightarrow Li_{1-x}CoO_2 + xLi^+ + xe^-$

Anode: $nC + xLi^+ + xe^- \leftrightarrow Li_xC_n$

Total: $LiCoO_2 + nC \leftrightarrow Li_{1-x}CoO_2 + Li_xC_n$

Lithium-ion batteries have the following advantages over other rechargeable batteries.

- high voltage
- high specific energy, light weight, small volume
- wide operation temperature range
- large specific power, large current discharge
- good cycle performance, long life

- no memory effect
- environment friendly, green source

Thus, lithium-ion batteries have been widely used in potable electronic devices such as mobile phones, laptops, and digital cameras, etc.

1.2 All solid-state battery

1.2.1 Demands for all solid-state batteries

In spite of the advantages described above, lithium-ion batteries are facing safety issues due to the risk of leakage and flammability of liquid organic electrolytes [13, 15]. When the batteries are overcharged, the electrolyte species are decomposed with gasing and increasing the cell temperature, which could cause an explosion. These issues are becoming more serous in lithium ion batteries when applied for large scale devices such as electric vehicles and load-leveling apparatuses. To address these issues, the development of all-solid-state lithium batteries using inflammable solid electrolytes has been anticipated [16, 17].

1.2.2 Advantage of all solid-state batteries

Figure 2 shows the schematic diagram of bulk-type all solid-state lithium-ion batteries using sulfide solid electrolyte [18]. Battery reaction proceeds by lithium intercalation, which is same with traditional lithium-ion batteries. The advantages of all solid-state lithium-ion batteries are as follows:

1. Extreme reliability: No leakage, vaporization and combustion of solid electrolytes. It absolutely needs for large-scale application.
2. High energy density: Solid-electrolytes have a wide potential window [12-14], which could enable to apply high capacity cathodes with high reaction voltages.
3. Ideally high current drain: Lithium ion is the sole conductive specie in solid-electrolytes, which should provide a fast reaction field. No other species diffuse to the electrode surface to take part in the side reactions [19].

4. High volume density: Bipolar stack structure of cells has a higher energy density than organic liquid electrolyte battery as shown in Figure 3 [20].

Based on these virtues, research of all solid-state battery began start. In the early stage, it is the history of materials research of highly conductive ionic conductors. After some lithium ion conductors with high conductivities were developed as the solid-electrolyte in all solid-state batteries, large electrochemical resistance at the solid/solid interface has been focused as another issue, which should be addressed.

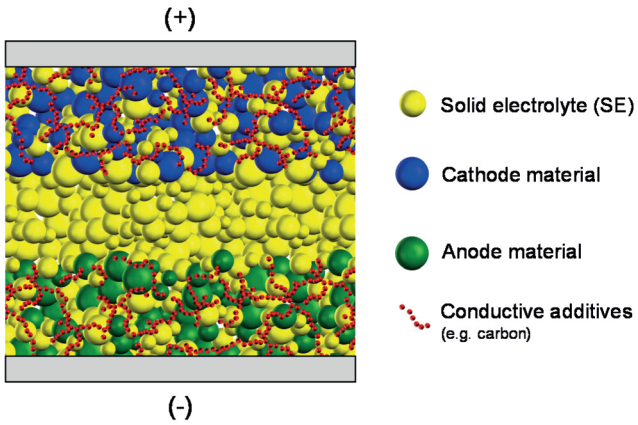

Figure 2. Schematic diagram of bulk-type all solid-state lithium battery using sulfide solid electrolyte [18].

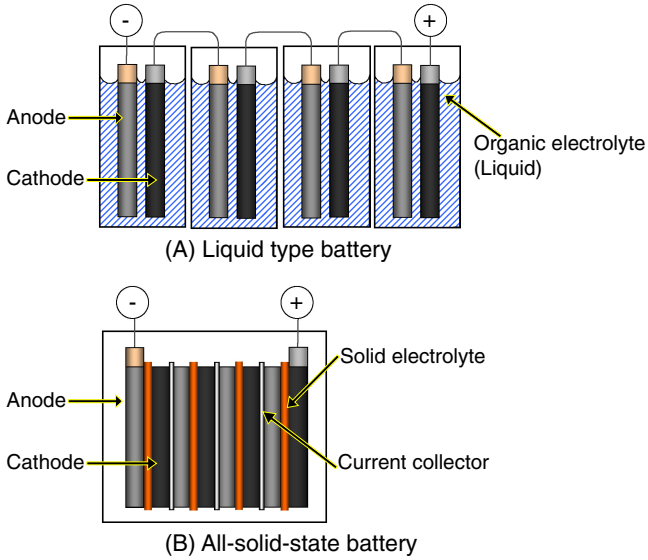

Figure 3. Outline of battery packages of (a) liquid type battery and (b) all solid-state battery [20].

1.3 Solid electrolytes for all solid-state batteries

1.3.1 Classification

Solid electrolytes are divided two kinds by polymeric and inorganic electrolytes. Polymer electrolytes contain solid polymer, gel polymer and polyionic liquid materials. The ionic conductivities are from 10^{-4} to 10^{-6} S cm^{-1} [21]. Polymer electrolytes have been used for hydrogen fuel cells and water electrolysis. However, some problems still do exist with polymeric systems like flammability and low ion conductivity at room temperature [22]. Inorganic electrolytes are divided to oxide and sulfide systems. Each system is divided to glass and crystalline systems.

1.3.2 Oxide systems

Lithium ion conductors with a LISICON (Li superionic conductor) type structure were developed in 1970-1980s such as $Li_{14}Zn(GeO_4)_4$, γ-Li_3PO_4, and Li_4SiO_4 [19, 23]. However, these materials show low ionic conductivity at room temperature. For example, the lithium ion conductivity of $Li_{3.6}Si_{0.6}P_{0.4}O_4$ is 5×10^{-6} S cm^{-1}. Amorphous $Li_{3.3}PO_{3.9}N_{0.17}$ (LiPON) has also the low conductivity 2×10^{-6} S cm^{-1} at room temperature. In contrast, the LiPON has a wide electrochemical window from 0 to 5.5 V [24]. Thus, the LiPON has been used as the solid electrolyte in thin film batteries, which shows excellent cycle performance [25]. $LiTi_2(PO_4)_3$ [26] and $Li_{1.3}Al_{0.3}Ti_{1.7}(PO_4)$ [27] with a NASCION-type structure and perovskite-type $Li_{3x}La_{2/3-x}TiO_3$ [28-30] have been reported to exhibit high ionic conductivities of over 10^{-3} S cm^{-1}. However, there are some technical issues to be addressed for the development of all solid-state batteries with these oxide solid electrolytes. First, Ti^{4+} ion is electrochemically instable against low voltage region below 2 V *vs.* Li. Second, oxide solid electrolytes show high grain boundary resistance [28, 31], although the bulk conductivities are enough high. Third, high interfacial resistance exists between oxide electrodes and those solid electrolytes [32, 33]. Thus, there is no bulk-type all solid-state batteries available for practical application.

1.3.3 Sulfide systems

Sulfide electrolytes have some advantages over the oxide electrolytes. First, sulfides show small grain boundary resistance for lithium diffusion, even in a cold-pressed pellet [34]. Second, sulfides have higher ionic conductivity because sulfide ions have larger ionic radii and more polarizable character improve the mobility of the conducting species [35]. Table 1 summaries sulfide solid electrolytes and their ionic conductivity [19].

Glass and glass-ceramic sulfide electrolytes in the Li_2S-P_2S_5 system have been reported to exhibit ionic conductivities of 10^{-5}~10^{-3} S cm^{-1} such as $75Li_2S{\cdot}25P_2S_5$ [39], $70Li_2S{\cdot}30P_2S_5$ [39], $80Li_2S{\cdot}20P_2S_5$ [36] glasses and $70Li_2S{\cdot}29P_2S_5{\cdot}1P_2S_3$ glass-ceramics [37]. Bulk-type all solid-state batteries have been developed with these sulfide electrolytes [38-40].

Crystalline materials should have higher conductivity than the corresponding glasses, if their crystal structures have been well designed for high ionic conduction [35]. The material design of crystalline ionic conductors is based on certain structural criteria: (1) mobile ions should have a suitable size for conduction pathways in the lattice, (2) there should be disorder in a mobile ion sublattice, and (3) highly polarizable mobile ions and anion sublattices are preferable [35, 41]. Based on the criteria, thio-LISICON family was discovered found on 2000 [42]. The thio-LISICON family is expressed by a general formula, Li*4-xM1-yM'y*S*4* with *M*= Si, Ge and *M'*= P, Al, Zn, Ga, and the substitutions of aliovalent cations improve the ionic conductivity [43]. Among the thio-LISICONs, $Li_{4-x}Ge_{1-x}P_xS_4$ (x= 0.75) shows ionic conductivity 2.2×10^{-3} S cm^{-1} [35]. Recently, new super ionic conductor sulfide $Li_{10}GeP_2S_{12}$ (LGPS) was developed. The $Li_{10}GeP_2S_{12}$ shows the highest ionic conductivity 1.2×10^{-2} S cm^{-1} at room temperature [44]. The LGPS has a three-dimensional structure, which is constructed by $(Ge_{0.5}P_{0.5})S_4$ tetrahedra, PS_4 tetrahedra, LiS_4 tetrahedra, and LiS_6 octahedra. The anisotropic conduction of Li^+ ions is along one crystal direction, namely through partially occupied LiS_4 tetrahedra and interstitial positions that are connected by a common edge, which is a characteristic of superionic conductors [44, 53]. The LGPS has been reported to have advantages of

chemical and electrochemical stability, and high ionic conductivity over previous sulfide electrolytes. Figure 4 shows the view of the all-solid-state lithium-ion battery with LGPS electrolyte. During charging, lithium ions (grey balls) with high mobility move from the positive $LiCoO_2$ electrode to the negative indium electrode through the LGPS electrolyte [53]. However, there has been few report about all solid-state batteries with the LGPS-type electrolytes.

Table 1 Conductivities at room temperature of sulfide solid electrolytes.

Solid electrolyte	Conductivity (S cm^{-1})
Glassy materials	
$0.5Li_2S–0.5\ GeS_2$ [45]	4.0×10^{-5}
$0.66Li_2S–0.33P_2S_5$ [46]	10^{-4}
$0.45LiI–0.37Li_2S–0.18P_2S_5$ [46]	1.7×10^{-3}
$Li_2S–B_2S_3$ [47]	10^{-4}
$0.44LiI–0.30Li_2S–0.26B_2S_3$ [47]	1.7×10^{-3}
$0.5Li_2S–0.5SiS_2$ [48]	1.2×10^{-4}
$0.3LiCl–0.35Li_2S–0.35SiS_2$ [48]	2.7×10^{-4}
$0.40LiI\text{-}0.36Li_2S\text{-}0.24SiS_2$ [49]	1.8×10^{-3}
$0.6Li_2S–0.4SiS_2$ [50]	5.0×10^{-4}
$0.3LiI–0.42Li_2S–0.28SiS_2$ [50]	8.2×10^{-4}
$0.01Li_3PO_4–0.63Li_2S–0.36SiS_2$ [51]	1.5×10^{-3}
$0.6Li_2S–0.4SiS_2$ [52]	1.5×10^{-4}
Crystalline materials	
$Li_{3.25}Ge_{0.25}P_{0.75}S_4$ [35]	2.2×10^{-3}
$Li_{10}GeP_2S_{12}$ [44]	1.2×10^{-2}
Li_6PS_5Cl [89]	1.33×10^{-3}
$Li_7P_3S_{11}$ [90]	3.2×10^{-3}
$Li_{3.25}P_{0.9}5S_4$ [91]	3.2×10^{-3}

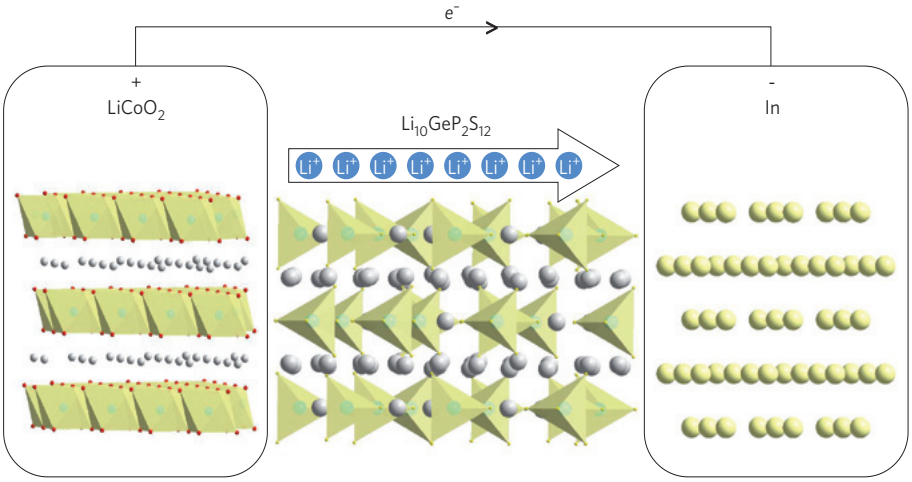

Figure 4. Schematic view of the all solid-state lithium-ion battery [53].

1.4 Electrodes for all solid-state batteries

1.4.1 Cathodes

Oxide and sulfide materials have been proposed as the cathode in all solid-state batteries such as $LiCoO_2$, $LiNi_xMn_yO_4$ [54], $LiMn_2O_4$ [55, 56], Li_2FeSiO_4 [57], TiS_2 [58, 59], and Li_3PS_4 [60]. $LiCoO_2$ is the most famous cathode, which has high operating voltage up to 4.2 V (*vs.* Li/Li^+) and high specific energy. Although there are many reports about $LiCoO_2$ cathode all solid-state battery [16, 20, 38-40, 61-63], very few reports have been available for the batteries using LGPS-type electrolytes. In this study, $LiCoO_2$ and TiS_2 will be focused on as cathodes in all solid-state batteries with the LGPS electrolyte.

$LiCoO_2$: Electrochemical lithium intercalation into $LiCoO_2$ was reported by Goodenough *et al* [64]. $LiCoO_2$ has a layered rocksalt-type structure where oxide ions adopt a cubic close-packed arrangement with Co^{3+} ions occupying octahedral sites between adjacent oxide ion layers (Figure 5) [15, 65]. When lithium ions deintercalate from $Li_{1-x}CoO_2$ in the region of $0 \leq x \leq 0.5$, the lattice slightly expands along the *c* axis and shows no significant change in the *a* and *b* axes. The small change in the host lattice leads to highly reversible structural changes during electrochemical

deintercalation/intercalation cycling [67]. The $LiCoO_2$ cathode delivers a highly reversible capacity of 130 mAh g^{-1} in the composition range in lithium-ion batteries. Furthermore, the $LiCoO_2$ cathode exhibits high current drain. Thus, $LiCoO_2$ is used as the cathode in present lithium ion batteries.

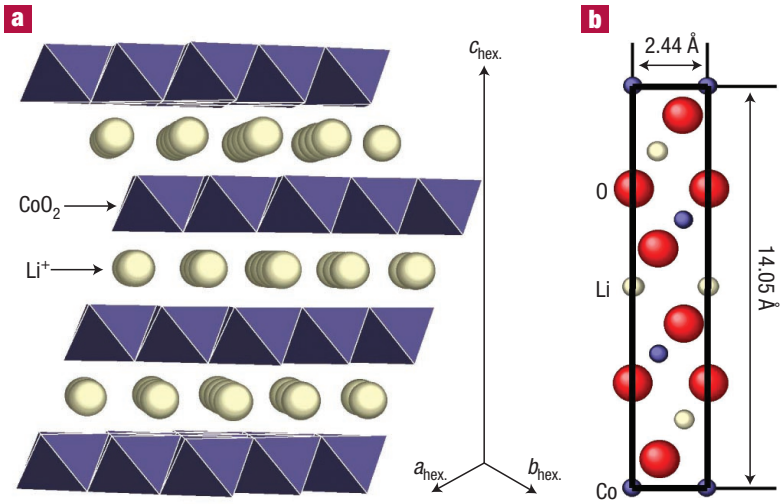

Figure 5. Crystal structure of layered rocksalt type $LiCoO_2$ [66].

TiS_2: TiS_2 has a hexagonal close-packed structure where each Ti is surrounded by six S in an octahedral structure. TiS_6 octahedra shared the edges to form a layered structure [68]. The individual layers of TiS_2 are bound together by van der Waals forces [65]. Li can intercalate into possible spaces between the TiS_6 layers [68] (Figure 6). The electrochemical reaction is as follows: $TiS_2 + Li+ + e- \rightleftarrows LiTiS_2$. The theoretical capacity is 239 mAh g^{-1}, which is much higher than that of $LiCoO_2$ (130 mAh g^{-1}). An all solid-state battery of TiS_2 with a glass sulfide electrolyte has been reported to deliver the first discharge capacity over 200 mAh g^{-1} [58].

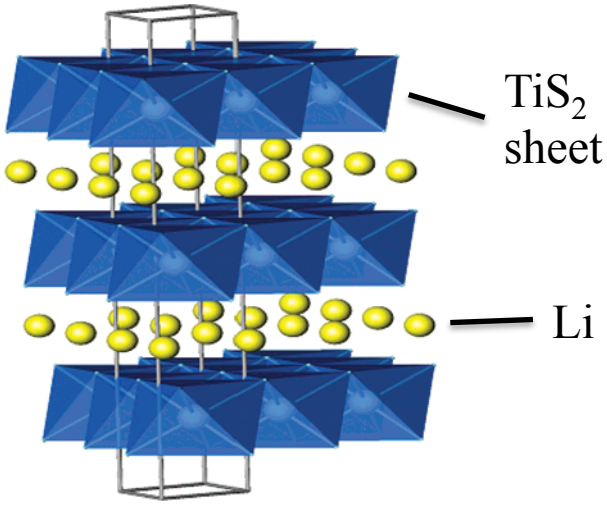

Figure 6. Crystal structure of Li_xTiS_2 [65].

1.4.2 Anodes

Various types of anode materials have been proposed for all solid-state batteries such as carbon [76], Li [77], In [38], In-Li alloy [78] and $Li_4Ti_5O_{12}$ [79]. The lithium anode has a very low potential, leading to a high operating voltage of the batteries. However, most of the solid electrolytes could be decomposed under the low potential. Furthermore, growth of the lithium dendrite causes short circuit of the batteries during the electrochemical cycling. The Li-*M* alloys (*M*= In, Al, Sn, Si, Ge) have been widely investigated as the anode in all solid-state battery. Table 2 summaries the capacity and the reaction potential of the anodes used with different solid electrolytes [19]. The In-Li alloy anode has a specific capacity of 180 mAh g^{-1}. The In-Li alloy formation from In proceeds at a potential of around 0.6 V *vs*. Li, which could suppress side reactions at the electrochemical interface such as the decomposition of solid electrolytes. Thus, the In-Li alloy shows a high coulombic efficiency of almost 100 % [78]. Interfacial resistances between anode and electrolyte have been reported to be relatively small compared to oxide cathode side interfaces. Glasses and crystalline-type electrodes have very high capacities. The electrochemical reaction proceeds by conversion reaction, which is the redox reaction between the transition metal the corresponding transition

metal oxide. However, the conversion electrodes show severe capacity fading during the charge-discharge [80, 81, 88].

Table 2 Capacities and reaction potentials of anodes for all solid-state batteries.

Anode	Solid electrolyte	Capacity (mAh g^{-1})	Potential (V *vs*. Li/Li^+)
Alloys			
In-Li [78]	Li_2S-SiS_2-Li_3PO_4 glass	180	0.6
Ge_xSi_{1-x} [82]	Li_2S-SiS_2 glass	190	0.5
Glasses			
SnO-B_2O_3 [83]	Li_2S-SiS_2-Li_3BO_3 glass	650	0.5
SnS-P_2S_5 [84]	Li_2S-P_2S_5 glass ceramics	600	0.5
Crystals			
Li_2FeS_2 [85]	Li_2S-SiS_2-Li_3PO_4 glass	400	1.6
FeS [86]	$Li_{3.25}Ge_{0.25}P_{0.75}S_4$	450	1.6
NiP_2 [87]	Li_2S-P_2S_5 glass ceramics	600	0.5
Li_2SiS_3 [88]	Li_2S-P_2S_5 glass ceramics	1200	1.5

1.5 Electrochemical activity of composite electrodes

The electrochemical reaction in bulk-type all solid-state batteries initiates at the point of contact interface between the particles of the electrode and the solid electrolyte. The reaction rate is limited due to a contact area at the interface. To secure the contact points of the particles, the positive electrodes for all solid-state batteries are composed of an active material together with a solid electrolyte using mechanical milling which leads to the highly-efficient utilization of the active material [16, 20, 40, 55, 61-63]. The best contact situation of active material and solid electrolyte is every active material particle could contact with solid electrolyte, which means solid electrolyte disperse around

active material to become a homogeneous dispersion system. This situation requires a high demand for particle size of active material and solid electrolyte. And the mix condition also could influence the contact area of them, especially, mix speed, mix time and the mill ball size. These conditions make sure active material and solid electrolyte particles could not aggregate by themselves or over disperse with each other.

So improve the composite condition is very important to fabricate composition cathode. However, there have been few reports investigating all solid-state batteries incorporating LGPS electrolytes, so little is know about the key factors associated with the fabrication process that may be able to improve the battery performance. In this thesis the composite cathode mixing conditions will be discussed to provide effective data for preparing composite cathode. Figure 9 is the schematic diagram of typical all solid-state battery, which shows a composite electrode composed of cathode particles and solid electrolyte particles is used as a working electrode to provide a lithium ion conductive path to the cathode [40].

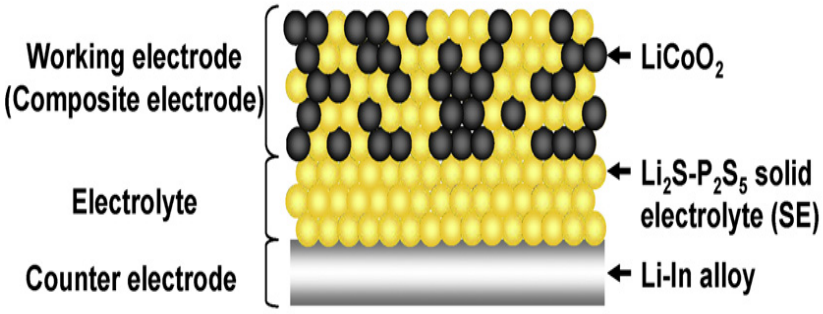

Figure. 9 Schematic diagram of typical all solid-state battery with composite cathode [40].

The electrochemical reaction in the composite electrodes initiates at the between the electrode and the solid electrolyte. It has been recognized that a highly-resistive layer is formed at oxide electrode/sulfide electrolyte interfaces during the electrochemical process, which limits the current density of the batteries. Mechanisms of the high interfacial resistance have been proposed as follows.

1) Space charge layer formation [16, 19, 56]: Lithium ions diffuse at the oxide electrode and sulfide electrolyte interface due to the difference in electrochemical potentials. As lithium ions have a higher electrochemical potential in sulfide lattices compared to oxide lattices, lithium ions diffuse from the sulfide electrolyte to the oxide electrode to decrease the difference in electrochemical potentials. The lithium depletion region is formed in the sulfide-side interface prior to the electrochemical cycling and is considered to lead to a high resistance for lithium diffusion at the interface.
2) Interfacial reaction during the initial electrochemical cycle [38]: An interfacial layer is formed at the initial charge-discharge reactions. Figure 7 shows the TEM/EDX images of an interfacial layer between oxide cathode $LiCoO_2$ and sulfide electrolyte $Li_2S{\cdot}P_2S_5$ after the initial charging. The TEM image confirms the formation of the interfacial layer with a thickness of about 10 nm. Both Co and P atoms are observed in the interfacial layer from the EDX line profiles. These results indicate that the interfacial layer is formed by mutual diffusion of cations between the oxide electrode and the sulfide electrolyte.

The formation of the resistive layer can be suppressed by surface coating of active materials with lithium metal oxides such as $Li_4Ti_5O_{12}$[16], $LiNbO_3$[61], $LiTaO_3$[63], Li_2SiO_3[38], Li_2ZrO_3[69], and $LiAlO_2$[70]. These materials are coated in amorphous states due to their higher lithium ion conductivity than that in crystalline states, since the lithium ions must diffuse in the coating layer at the electrochemical process. The roles of the coating layer have been considered as follows: 1) Decreasing the difference in the electrochemical potentials of lithium, which eliminates the space charge layer formation between the oxide electrode and the sulfide electrolyte. 2) Suppressing the direct contact of the oxide electrode with the sulfide electrolyte, which eliminates the mutual diffusion of cations between the oxide electrode and the sulfide electrolyte. Figure 8 shows the cross-section TEM image of Li_2SiO_3-coated $LiCoO_2/Li_2S{\cdot}P_2S_5$ solid electrolyte interface after the first charging. No interfacial layer is observed after the

electrochemical reaction, leading to a low interfacial resistance. Ohta *et al.* have reported that the interfacial resistance of $LiNbO_3$-coated $LiCoO_2$ depends on the thickness of $LiNbO_3$ coating layer [61].

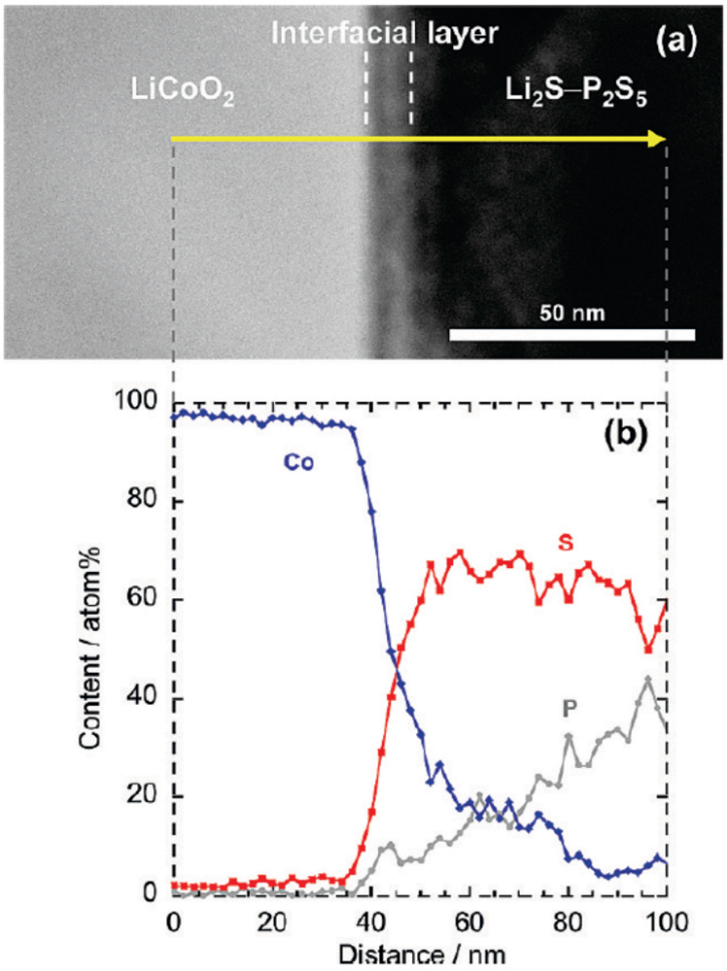

Figure 7. (a) Cross-section HAADF-STEM image of $LiCoO_2$ electrode/ $Li_2S{\cdot}P_2S_5$ solid electrolyte interface after initial charging and (b) cross-sectional EDX line profiles for Co, P, and S element [38].

Table 3 summarizes various surface-coating oxide cathodes and their rate-capability in all solid-state batteries with sulfide solid electrolytes. The interfacial resistances depend on the combination of active material, coating species, and sulfide electrolyte. Whereas the interfacial reactions of oxide cathodes with Li_2S–P_2S_5 glass and thio-LISICON type

sulfide electrolytes have been investigated, no reports have been available regarding to the interface between oxide electrodes and LGPS-type electrolytes.

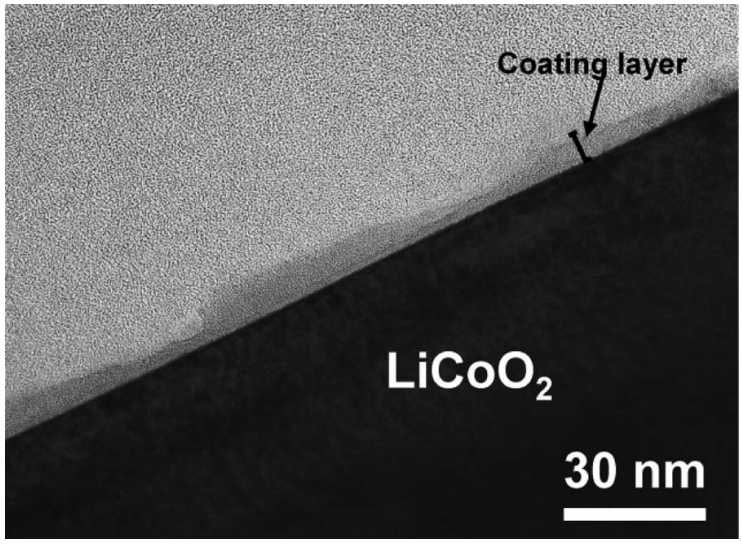

Figure 8. Cross-sectional TEM image of 0.6 wt % Li_2SiO_3-coated $LiCoO_2$ particles [38].

Table 3 Surface-coating enhancing the rate-capability of oxide cathodes in sulfide solid electrolytes.

Buffer layer	Oxide cathode	Sulfide SE	Electrode resistance (Ω)
$Li_4Ti_5O_{12}$ [16]	$LiCoO_2$	$Li_{3.25}Ge_{0.25}P_{0.75}S_4$	44
$LiNbO_3$ [61]	$LiCoO_2$	$Li_{3.25}Ge_{0.25}P_{0.75}S_4$	＜20
Li_2O–SiO_2 [71]	$LiCoO_2$	$80Li_2S$–$20P_2S_5$	160
$LiTaO_3$ [63]	$LiCoO_2$	$Li_{3.25}Ge_{0.25}P_{0.75}S_4$	＜20
$Li_2Ti_2O_5$ [72]	$LiCoO_2$	$80Li_2S$–$20P_2S_5$	100
Li_4SiO_4–Li_3PO_4 [73]	$LiCoO_2$	$80Li_2S$–$20P_2S_5$	48
$Li_4Ti_5O_{12}$ [74]	$LiNi_{1/3}Co_{1/3}Mn_{1/3}O_2$	$80Li_2S$–$19P_2S_5$–$1P_2O_5$	100
Li_4Ti5O_{12} [55]	$LiMn_2O_4$	$80Li_2S$–$20P_2S_5$	100
Li_4Ti5O_{12} [75]	$LiNi_{0.8}Co_{0.15}Al_{0.05}O_2$	$70Li_2S$–$30P_2S_5$	48

1.6 Purpose of this study

The purpose of the study is to develop composite electrodes with the LGPS electrolyte for all solid-state batteries. Although the composite electrodes have been widely used for the cathodes in all solid-state batteries, very few reports have been available for the use of the LGPS as the solid-electrolyte, despite its extremely high ion conductivity. It is therefore importance of clarifying how the structures of the composite electrodes affect the all solid-state battery performance. Furthermore, electrochemical reactions of composite electrodes should depend on the electrode material. In this thesis, $LiCoO_2$/LGPS and TiS_2/LGPS are focused on as oxide/sulfide and sulfide/sulfide composites, respectively. As described in the above sections, $LiCoO_2$ has been widely used with other solid-electrolytes for all solid-state batteries. The $LiCoO_2$/LGPS composites could provide direct information regarding to the suitability of the LGPS as the solid-electrolyte. In contrast, the TiS_2/LGPS could evaluate the diversity of cathode materials used with the LGPS and clarify the difference of interfacial reactions between oxide/sulfide and sulfide/sulfide interfaces. The present study consists of the following two experimental steps for different cathode materials:

1. Fabrication and structural characterization of $LiCoO_2$/LGPS and TiS_2/LGPS composite cathodes with different mixing conditions and surface modification.
2. Electrochemical investigation of $LiCoO_2$/LGPS and TiS_2/LGPS composite cathodes

The results in the present study are briefly summarized as follows.

In chapter 3, composite cathodes consisting of $LiCoO_2$ and LGPS were fabricated under various conditions to clarify the key parameters for high electrochemical activity. Mild mixing condition, small particle size of LGPS leaded to the well-dispersed composites with high contact area between $LiCoO_2$ and LGPS. Surface coating of

$LiNbO_3$ on the $LiCoO_2$ surface coating decreased the resistance of the charge transfer reaction.

In chapter 4, TiS_2/LGPS composites were fabricated and their electrochemical properties were investigated. The TiS_2/LGPS composite prepared under the optimized mixing condition exhibited higher initial charge/discharge capacities than the $LiCoO_2$/LGPS composite. However, severe capacity fading was caused by the decrease in physical contact between TiS_2 and LGPS, which was induced by the large lattice change of TiS_2 during lithium (de)intercalation. Applying a pressure to the cells during the electrochemical cycling drastically improved the cycle retention and the rate capability of the TiS_2/LGPS composites. The volume change in the composites is the key for achieving stable battery operation.

These results reveal the optimized conditions for fabricating well-dispersed composites of $LiCoO_2$/LGPS and TiS_2/LGPS and the importance of applying cell pressure to secure contact area between the cathodes and the LGPS solid-electrolyte. The $LiCoO_2$/LGPS and TiS_2/LGPS composites deliver highly reversible electrochemical reactions, which demon stares that the LGPS is one of the most promising electrolytes for the cathode composites in all solid-state batteries.

References

[1] M.S. Whittingham, *Scinece*, 192 (1976) 1126.

[2] M.S. Whittingham, US patent 4009052.

[3] M.B. Armand, Materials for Advanced Batteries (Proc. NATO Symp. Materials Adv. Batteries) (eds D.W. Murphy, J. Broadhead & B.C.H. Steele) 145-161 (Plenum, New York, 1980).

[4] D.W. Murphy, F.J. Disalovo, J.N. Carides & J.V Waszczak, *Mat. Rev. Bull.,* 13 (1978) 1395.

[5] M. Lazzari & B.A. Scrosati, *J. Electrochem. Soc.,* 127 (1980) 773.

[6] J.M. Tarascon & M. Armand, *Nature,* 414 (15) (2001) 359.

[7] J.S. Kim, C.S. Johnson, M.M. Thackeray, *Electrochem Commun.*, 4 (2002) 205.

[8] H. Kobayashi, R. Kanno, M. Tabuchi, H. Kageyama, O. Nakamura, M. Takano, *J. Power Sources*, 68 (1997) 686.

[9] B. Ammundsen, J. Paulsen, I. Davidson, R.-S. Liu, C.-H. Shen, J.-M. Chen, L.-Y. Jang, J.-F. Lee, *J. Electrochem. Soc.*, 149 (2002) A431.

[10] S.S. Shin, Y.K. Sun, K. Amine, *J. Power Sources*, 112 (2002) 634.

[11] F. Orsini et al. *J. Power Sources,* 81–82 (1999) 918.

[12] T. Nagaura, Paper presented at *4th Int. Rechargeable Battery Seminar,* Deerfield Beach, FL, 1990; T. Nagaura and K. Tazawa, *Prog. Batteries Col. Cells,* 9 (1990) 20.

[13] P. G. Bruce, *Philos. Trans. R. Soc. Lond. A,*. 354 (1996), 1577.

[14] K. Ozawa, *Solid State Ionics,* 69 (1994) 212.

[15] P.G. Bruce, *Chem. Commun.*, (1997) 1817.

[16] N. Ohta, K. Takada, L.Q. Zhang, R.Z. Ma, M. Osada, T. Sasaki, *Adv. Mater.*, 18 (2006) 2226.

[17] A. Sakuda, H. Kitaura, A. Hayashi, K. Tadanaga, M. Tatsumisago, *J. Electrochem. Soc.,* 156 (2009) A27.

[18] Y.S. Jung, D.Y. Oh, Y.J. Nam, K.H. Park, *Isr. J. Chem.*, 55 (2015), 472.

[19] K. Takada, *Acta Materialia*, 61 (2013) 759.

[20] Y. Kato, K. Kaeamoto, R. Kanno, M. Hirayama, *Electrochemistry*, 80 (2012) 749.

[21] M.S. Su'ait, M.Y.A. Rahman, A. Ahmad, *Solar Enegy,* 115 (2015) 452.

[22] J.G. Kim, B. Son, S. Mukherjee, N. Schuppert, A. Bates, O. Kwon, M.J. Choi, H.Y. Chung, S. Park, *J. Power Sources,* 282 (2015) 299.

[23] HY-P Hong, *Mater Res Bull*, 13 (1978) 117.

[24] X.H. Yu, J.B. Bates, G.E. Jelison, Jr, F.X. Hart, *J. Electrochem Soc.*, 144 (1997)524.

[25] B. Wang, J.B. Bates, F.X. Hart, B.C. Sales, R.A. Zuhr, J.D. Robertson, *J. Electrochem.Soc.*, 143 (1996) 3203.

[26] H. Aono, E. Sugimoto, Y. Sadaoka, N. Imanaka, G. Adachi, *J. Electrochem.Soc.,* 136 (1989) 590.

[27] H. Aono, E. Sugimoto, Y. Sadaoka, N. Imanaka, G. Adachi, *J. Electrochem.Soc.,* 137 (1990) 1023.

[28] Y. Inaguma, C. Liquan, M. Itoh, T. Nakamura, T. Uchida, H. Ikuta et al, *Solid State Commun.*, 86 (1993) 689.

[29] A. Astiq, M. Menetrier, L. Croguennec, E. Suard, C. Delmas, *J. Mater. Chem*, 12 (2002) 2971.

[30] M. Klingler, W.F. Chu, W. Weppner, *Ionics*, 3 (1997) 289.

[31] H. Aono, E. Sugimoto, Y. Sadaoka, N. Imanaka, G. Adachi, *Solid State Ionics*, 47 (1991) 257.

[32] A. Sakuda, A. Hayashi, M. Tatsumisago, *Sci. Rep.*, 3 (2003) 2261.

[33] M. Kotobuki, H. Munakata, K. Kanamra, Y. Sato, T. Yoshida, *J. Electrochem. Soc*, 157 (2010) A1076.

[34] K. Takada, S. Kondo, *Ionics*, 4 (1998) 42.

[35] R. Kanno, M. Murayama, *J. Electrochem. Soc.*, 148 (2001) A742.

[36] T. Minami, A. Hayashi, M. Tatsumisago, *Solid State Ionics*, 177 (2006) 2715.

[37] M. Tatsumisago, A. Hayashi, *Solid State Ionics*, 225 (2012) 342.

[38] A. Sakuda, A. Hayashi, M. Tatsumisago, Chem. Mater, 22 (2010) 949.

[39] T. Ohtomo, A. Hayashi, M. Tatsumisago, Y. Tsuchida, S. Hama, K. Kawamoto, *J. Power Sources*, 233 (2013) 231.

[40] A. Sakuda, A. Hayashi, T. Ohtomo, S. Hama, M. Tatsumisago, *J. Power Sources*, 196 (2011) 6735.

[41] A.R. West, in Basic Solid State Chemistry, 2nd ed., Chap. 7.5, p. 321, John Wiley & Sons, Chichester, U.K. (1999).

[42] R. Kanno, T. Hata, Y. Kawamoto, M. Irie, *Solid State Ionics*, 130 (2000) 97.

[43] M. Murayama, R. Kanno, Y. Kawamoto, T. Kamiyama, *Solid State Ionics*, 154-155 (2002) 789.

[44] N. Kamaya, K. Homma, Y. Yamakawa, M. Yonemura, T. Kamiyama, Y. Kato, S. Hama, K. Kawamoto, A. Mitsui, M. Hirayama, R. Kanno, *Nature. Mater.,* 10 (2011) 682.

[45] M. Ribes, B. Barrau, J.L. Souquet, *J. Non-Cryst Solids*, 38 (1980) 271

[46] R. Mercier, J.P. Malugani, B. Fahys, G. Robert, *Solid State Ionics*, 5 (1981) 663.

[47] H. Wada, M. Menetrier, A. Levasseur, P. Hagenmuller, *Mater Res Bull*, 18 (1983) 189.

[48] J.H. Kennedy, S. Sahami, S.W. Shea, Z. Zhang, *Solid State Ionics*, 18-19 (1986) 368.

[49] J.H. Kennedy, Y. Yang, *J. Electrochem Soc*, 133 (1986) 2437.

[50] A. Pradel, M. Ribes, *Solid State Ionics*, 18-19 (1986) 351.

[51] N. Aotani, K. Iwamoto, K. Takada, S. Konda, *Solid State Ionics*, 68 (1994) 35.

[52] H. Morimoto, H. Yamashita, M. Tatstmisago, T. Minami, *J. Amceram Soc*, 82 (1999) 1352.

[53] C. Masquelier, *Nature Mater.*, 10 (2011) 649.

[54] A.G. Gao, K. Sun, L.N. Cong, Y.H. Zhang, Q. Zhao, R.S. Wang, H.M. Xie, L.Q. Sun, Z.M. Su, *J. Alloys Compd.*, 654 (2016) 257.

[55] H. Kitaura, A. Hayashi, K. Tadanaga, M. Tatsumisago, *Solid State Ionics*, 192 (2011) 304.

[56] K. Takada, N. Ohta, L.Q. Zhang, X.X. Xu, B.T. Hang, T. Ohnishi, M. Osada, T. Sasaki, *Solid State Ionics*, 225 (2012) 594.

[57] R. Tan, J. Yang, J. Zheng, K. Wang, L. Lin, S. Ji, J. Liu, F. Pan, *Nano Energy*, 16 (2015) 112.

[58] J. E. Trevey, C. R. Stoldt, S.-H. Lee, *J. Electrochem. Soc.*, 158 (2011) A1282.

[59] B. R. Shin, Y. J. Nam, D. Y. Oh, D. H. Kim, J. W. Kim, Y. S. Jung, *Electrochim. Acta.*, 146 (2014) 395.

[60] T. Hakari, M. Nagao, A. Hayashi, M. Tatsumisago, *J. Power. Sources*, 293 (2015) 721.

[61] N. Ohta, K. Takada, I. Sakaguchi, L. Zhang, R. Ma, K. Fukuda, M. Osada, T. Sasaki, *Electrochem. Commun.*, 9 (2007) 1486.

[62] A. Sakuda, H. Kitaura, A. Hayashi, K. Tadanaga, M.J. Tatsumisago, *Electrochem. Soc.*, 156 (2009) A27.

[63] K. Takada, N. Ohta, L. Zhang, K. Fukuda, I. Sakaguchi, R. Ma, M. Osada, T. Sasaki, *Solid State Ionics*,179 (2008) 1333.

[64] K. Mizushima, P. C. Jones, P. J. Wiseman, J. B. Goodenough, *Mat. Res. Bull.*, 15 (1980) 738.

[65] M.S. Whittingham, *Chem. Rev.*, 104 (2004) 4271.

[66] Y.S. Horn, L. Croguennec, C. Delmas, E.C. Nelson and M.A. O'Keefe, *Nature Mater.*, 2 (2003) 464.

[67] G. G. Amatucci, J. M. Tarascon, C. Kleinb, *J. Electochem. Soc.*, 143 (1996) 1113.

[68] S. N. Patel, A. A. Balchin, *Zeitschrift fur Kristallographie.*, 164 (1983) 273.

[69] S. Ito, S. Fujiki, T. Yamada, Y. Aihara, Y. Park, T.Y. Kim, S.W. Baek, J.M. Lee, S. Doo, N. Machida, *J. Electochem. Soc.*, 248 (2014) 943.

[70] K. Okada, N. Machida, M. Naito, T. Shigematsu, S. Ito, S. Fujiki, M. Nakano, Y. Aihara, *Solid State Ionics,* 255 (2014) 120.

[71] A. Sakuda, H. Kitaura, A. Hayashi, K. Tadanaga, M. Tatsumisago, *Electrochem Solid-State Lett*, 11 (2008) A1.

[72] A. Sakuda, A. Hayashi, M. Tatsumisago, *J. Power Sources*, 195 (2010) 599.

[73] Y. Sakurai, A. Sakuda, A. Hayashi, M. Tatsumisago, *Solid State Ionics*, 182 (2011) 59.

[74] H. Kitaura, A, Hayashi, K. Tadanaga, M. Tatsumisago, *Electrochim Acta*, 55 (2010) 8821.

[75] Y. Seino, T. Ota, K. Takada, *J. Power Source*, 196 (2011) 6488.

[76] U. Kasavajjula, C. Wang, A.J. Appleby, *J. Power Sources*, 163 (2007) 1003.

[77] J.H. Woo, J.E. Trevey, A.S. Cavanagh, Y.S. Choi, S.C. Kim, S.M. George, K.H. Oh, S.H. Lee, *J. Electrochem. Soc.*, 159 (2012) A1120.

[78] K. Takada, N. Aotani, K. Iwamoto, S. Kondo, *Solid State Ionics*, 86-88 (1996) 877.

[79] H. Geng, A. Mei, Y. Lin, C. Nan, *Mater. Sci. Eng. B*, 164 (2009) 91.

[80] P, Poizot, S, Laruelle, S, Grugeon, L, Dupont, J.M. Tarascon, *Science*, 407 (2000) 496.

[81] D. Larcher, C. Masquelier, D. Bonnin, Y. Chabre, V. Masson, J.B. Leriche, *J. Electrochem. Soc.*, 150 (2003) A133.

[82] Y. Hashimoto, N. Machida, T. Shigematsu, *Solid State Ionics*, 175 (2004) 177.

[83] A. Hayshi, M. Nakai, M. Tatsumisago, T. Minami, M. Kanda, *J. Electrochem Soc.* 150 (2003) A582.

[84] A. Hayshi, T. Konishi, K. Tadanaga, T. Minami, M. Tatsumisago, *J. Power Sources*, 146 (2005) 496.

[85] K. Takada, Y. Kitami, T. Inada, A. Kajiyama, M. Kouguchi, S. Kondo et al, *J. Electrochem Soc*, 148 (2001) A1085.

[86] B.C. Kim, K. Takada, N. Ohta, Y. Seino, L.Q. Zhang, H. Wada et al, *Solid State Ionics*, 176 (2005) 2383.

[87] A. Hayashi, A. Inoue, M. Tatsumisago, *J. Power Sources*, 189 (2009) 669.

[88] B.T. Hang T. Ohnishi, M. Osada, X.X. Xu, K. Takada, T. Sasaki, *J. Power Sources*, 195 (2010) 3323.

[89] S. Boulineau, M. courty, J.M. Tarascon, V. Viallet, *Solid State Ionics*, 221 (2012) 1.

[90] H. Yamane, M. Shibata, Y. Shimane, T. Junke, Y. Seino, S. Adams, K. Minami, A. Hayashi, M. Tatsumisago,

Chapter 2

Experiment

2.1 Synthesis of $Li_{10}GeP_2S_{12}$ (LGPS)

LGPS was synthesized by a solid-state reaction [1]. The starting materials were Li_2S (Idemitsu Kosan, >99.9 % purity), P_2S_5 (Aldrich, >99 % purity) and GeS_2 (Aldrich, >99 % purity). There were weighed, mixed in the molar ratio of $LiS_2/P_2S_5/GeS_2$ to 5/1/1 in an Ar-filled glove box, placed into a stainless-steel pot and mixed for 30 min using a vibrating mill (CMT, Tl-100). The specimens were then pressed into pellets, sealed in a quartz tube at a vacuum level of 30 Pa and heated at a reaction temperature of 400 °C for 8 h in a furnace. After reacting, the tube was slowly cooled to room temperature. The sample was ground and pressed, by 380 MPa and sealed in a quartz tube. The sample was resintered at 550 °C for 8 h. Figure 1 shows the sintering processes of fabricating LGPS (RT: room temperature, N.C: nature cooling, Air: air atmosphere). XRD (Rigatu, Smart Lab) measurement using Cu $K\alpha_1$ radiation was performed to confirm the formation of the single phase. The specimen was sealed in sample holder in a vacuum for the XRD measurements. Diffraction data were collected in 0.01° steps from 10° to 100° in 2 θ. Figure 2 shows the XRD pattern of the product. All diffraction peaks were attributed to $Li_{10}GeP_2S_{12}$ [1].

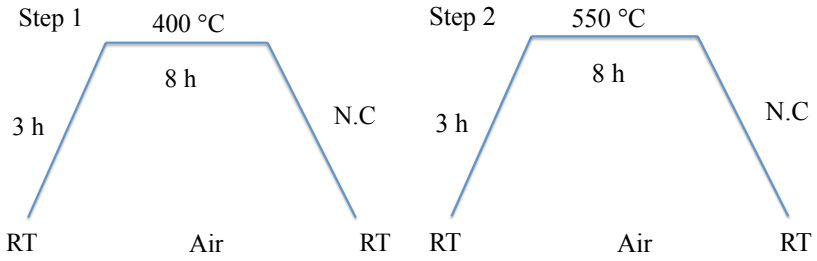

Figure 1. Sintering processes of LGPS.

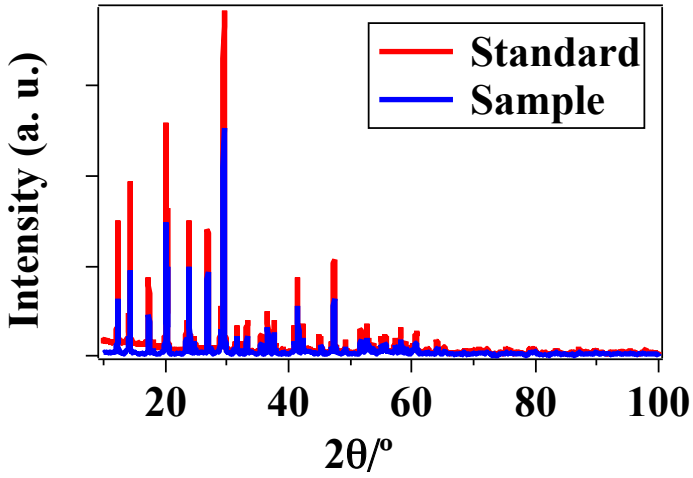

Figure 2. XRD patterns of $Li_{10}GeP_2S_{12}$.

2.2 Fabrication of all solid-state batteries with $LiCoO_2$ cathode

2.2.1 Surface coating of $LiNbO_3$ on $LiCoO_2$

The $LiCoO_2$ surface was coated with a thin $LiNbO_3$ layer using a fluidized bed granulator (Powrex, MP-01) to suppress formation of a highly resistive layer between the $LiCoO_2$ an LGPS. $LiCoO_2$ powder (500 g, average particle size (*d*50): 16.7 μm, surface area: 0.23 m g^{-1}) was used as the starting material. An ethanol alkoxide solution consisting of anhydrous ethanol (39.68 g), Li metal (0.23 g) and niobium pentaethoxide (10.96 g) was sprayed onto the $LiCoO_2$ at a rate of 2 g min^{-1}. The weight ratio of the coating layer to the $LiCoO_2$ was controlled by the duration of the spraying process. Each sample was annealed at 350 °C for 1 h in air to remove any organic contaminants. X-ray diffraction (XRD) patterns of pristine, coated and annealed samples were acquired with an X-ray powder diffract meter (Rigaku, Smart lab) using Cu $K\alpha_1$ radiation. The morphology of each sample was observed by SEM (VE-8600, Keyence).

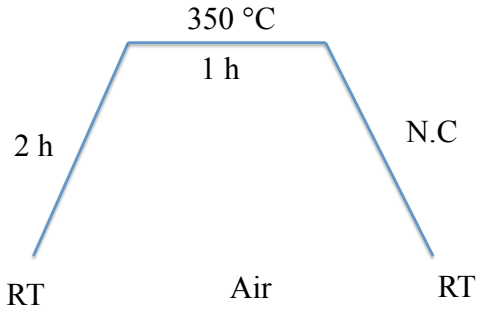

Fig. 3 Annealing process of $LiNbO_3$ coated $LiCoO_2$.

2.2.2 Preparation of $LiNbO_3$-coated $LiCoO_2$/LGPS composites

Composite positive electrodes of $LiNbO_3$-coated $LiCoO_2$ and LGPS were prepared of improve the lithium ion conduction between the $LiCoO_2$ and LGPS slid electrolyte. A mill pot rotator (ANZ-10S, Nitto) was used to fabricate the composites because this device allowed ready control over the mixing conditions, such as the rotating speed, grinding time, mill balls size and so on.

The ratio of $LiCoO_2$: LGPS is 70:30, which is tested by many reports before [2, 3]. The first step is deciding rotating speed. Prepare three samples with five 3 mmϕ mill balls, at different speed 140, 250 and 350 rpm for 10 min, and then fabricate solid-state battery with three samples to test the electrochemical performance of these samples, to choose suitable rotate speed. The second step is change mill ball size from 3 mmϕ to 5 mmϕ using 140 rpm speed mix LGPS and $LiCoO_2$ for 10 min, and then fabricate batteries to test the electrochemical performance, to find the fit ball size. The third step is LGPS particle size, grind LGPS manually in an agate mortar to decrease the particle size. Fabricate battery and composite cathode with LGPS samples and then test the electrochemical performance of solid-state batteries. The fourth step, prolong the composite cathode mixing time from 10 to 20 and 30 min to test samples' electrochemical properties. The last step is testing coating layers $LiNbO_3$ thickness, use ICP method calculate the thickness of $LiNbO_3$ and then go on the electrochemical test to find the best one. Finally, the composite cathode fabricated conditions are decided:

rotation rate is 140 rpm, mill ball size is 3 mmϕ, LGPS grinding time is 10 min, mixture grinding time is 30 min and the coating layer thickness of $LiNbO_3$ on $LiCoO_2$ around 0.5 wt.%. In this study, the battery with the composite cathode shows a very large discharge capacity about 125 mAh g^{-1}. The composite cathode fabrication process demonstrated that the fabricating conditions will strongly affect electrochemical performance of battery, so keep eye on composite cathode is very importance. Figure 4 shows the schematic of mill pot rotator and composite cathode fabricating process.

The morphology of all samples was observed by SEM (JSM-6610LV, JEOL).

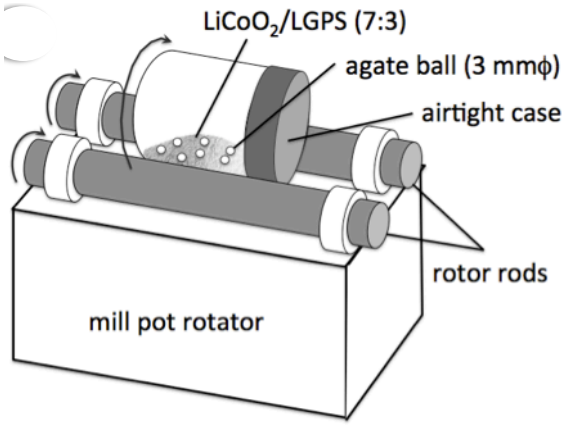

Figure 4. Schematic of mill pot rotator and composite cathode fabricating process.

2.2.3 Fabrication of $LiNbO_3/LiCoO_2$/LGPS/In-Li cells

Tow-electrode all solid-state batteries were used to investigate the electrochemical properties of the composites electrodes [4]. These batteries were fabricated using LGPS and In-Li metal as the solid electrolyte and the negative electrode, respectively. In making these batteries, a 100 mg sample of the LGPS electrolyte was pressed into a pellet with a 10 mm diameter and aluminum foil and aluminum mesh were employed as current collectors for the positive electrode. Composite electrode powder (10 mg) was pressed onto the LGPS electrolyte pellet at a pressure of 555 MPa. The negative electrode was composed of Li foil (5 mmϕ, 0.1 mmt) and In foil (10 mmϕ, 0.1 mmt) on a Cu mesh current collector. Finally, the three layers (positive electrode/electrolyte/

negative electrode) were pressed together under a pressure of 19 MPa to fabricate the all solid-state batteries. Figure 5 shows the schematic of three layered pressed all solid-state battery. All the above processes were performed in a dry Ar-filled glovebox (DBO-1.5-T1000, Miwa).

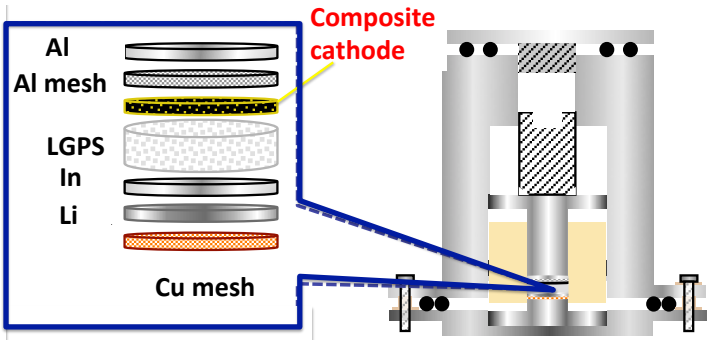

Figure 5. Schematic of all solid-state battery.

2.3 Fabrication of all solid-state batteries with TiS_2 cathode

2.3.1 Nanosizing of TiS_2

In order to increase the contact area between the TiS_2 and the LGPS solid-electrolyte, a high-energy ball mill (Fritsch pulverisette 7) was performed for commercial TiS_2 powder (Kojundo Chemical Laboratory Co. Ltd, Japan). The grinding condition was 320 rpm for 16 h. The crystal structure and morphology of the milled TiS_2 were verified using X-ray diffraction patterns (XRD: Smartlab CuKα, Rigaku). Brunaure-Emmett-Teller (BET: BELSORP-mini, MicrotracBEL) was conducted to verify the specific surface area of TiS_2 samples.

2.3.2 Preparation of TiS_2/LGPS composites

Composite cathodes were prepared to improve lithium ion conductive between the TiS_2 and the LGPS solid electrolyte. Vortex miller (TTM-1, SIBATA) (Figure 6) was used to fabricate composite cathode, which is a very popular and simple mixing method.

The weight ratio between TiS_2 and LGPS was 30:70. The rotate speed is 2500 rpm and the grinding time was 2, 5 and 10 min. Different durations of mixing were applied to find the condition for fabricating well-dispersed composites. The morphology of the composites was observed by SEM (JSM-6610LV, JEOL).

Figure 6. Picture of Vortex mixer.

2.3.3 Fabrication of TiS_2/LGPS/In-Li cells

The $Li_{10}GeP_2S_{12}$ electrolyte (100 mg) was prepared as a pellet with a 10 mm diameter. An aluminum foil and mesh were used as current collectors for the cathode. The cathode powder (10 mg) was pressed onto the $Li_{10}GeP_2S_{12}$ electrolyte pellet under 555 MPa. The negative electrode was consisted of Li foil (5 mmϕ, 0.1 mmt) and In foil (10 mmϕ, 0.1 mmt) on a copper mesh current collector. Finally, the three-layers of the cathode/electrolyte/anode were pressed together at 19 MPa to fabricate the all solid-state batteries. A pressure of 230 MPa was applied on the battery during the charge-discharge operation. All the processes for the solid-state batteries were performed in a dry Ar-filled glovebox (DBO-1.5-T1000, Miwa).

2.4 Inductively coupled plasma mass spectrometry (ICP-MS)

Inductively couple plasma mass spectrometry (ICP-MS) is an analytical technique used for elemental determinations, which was commercially introduced in 1983 and has gained general acceptance in many types of laboratories. It has many advantages including, greater speed, precision, sensitivity and the ability to obtain isotopic information. An ICP-MS combines a high temperature ICP source with a mass spectrometer. The ICP source converts the atoms of the elements in the sample to ions. These ions are then separated and detected by the mass spectrometer.[5]

In this study, ICP method was used to calculate the coating layer thickness by the content of $LiNbO_3$. Ten samples participated in ICP test. These samples have different $LiNbO_3$ content by changing the spray time. Every sample 10 mg dissolved in 10 ml hydrochloric acid (20 %) to make solution. Then diluted these solutions by 50 ml deionized water respectively and analysis by ICP equipment. From ICP results, Li, Co and Nb elements concentration (mg L^{-1}) could be known and the content of $LiCoO_2$, $LiNbO_3$ and thickness of $LiNbO_3$ could be calculated. Compare with the values analyzed from the amount of applied solution, ICP results are more precise which shows in Figure 7.

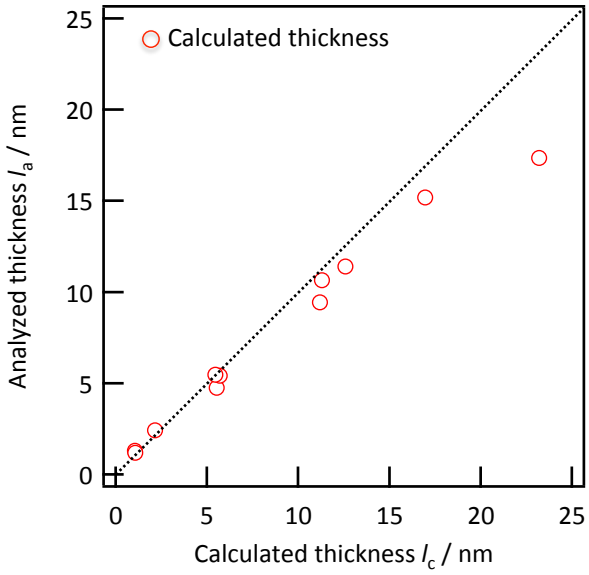

Figure 7. Analyzed thickness by applied solution and calculated thickness by ICP.

2.5 Electrochemical measurements

2.5.1 Charge-discharge test

$LiNbO_3$/$LiCoO_2$/LGPS/In-Li Charge/discharge measurements were performed at 25 °C outside glove-box using a multi-channel potentio/galvanostat (TOSCAT-3100, Toyo system). The upper and lower cutoff voltages were 3.6 V and 1.9 V, which could corresponds to 4.2 V and 2.5 V *vs.* Li/Li^+, respectively, Because the potential of the In-Li alloy is about 0.6 V higher than that of Li/Li^+, with an applied current rate of 7 mA g^{-1} (0.05 C). Specific capacities were calculated based on the active mass of $LiCoO_2$. The interfacial condition between the In/Li and the LGPS electrolyte gradually changed with the cycle number, as we will show later. The differences in the performance among composite cathodes were evaluated at the first cycle to minimalize effects of the anode condition on the charge/discharge capacity.

TiS_2/LGPS/In-Li Two types of test conditions were investigated to clarify effects of pressure on battery performance: 1) encasing the cell in a stainless steel container and 2) maintaining the cells under 228 MPa using the pressure instrument during the charge-discharge operation. The schematic of the pressed condition is shown in Figure 8. Charge/discharge measurements were performed at 25 °C inside or outside glove-box using a multi-channel potentio/galvanostat (TOSCAT-3100, Toyo system) and Solartron 1287. The upper and lower cutoff voltages were 2.5 V and 1.0 V, and the current densities were 0.088 mA cm^{-2} (0.1 C) to 1.76 mA cm^{-2} (2 C).

2.5.2 Impedance analysis

Electrochemical impedance spectroscopy (EIS) is a relatively new and powerful method of characterizing many of the electrical properties of materials and their interfaces with electronically conducting electrodes. The general approach is to apply an electrical stimulus (a known voltage or current) to the electrodes and observe the response (the resulting current or voltage).

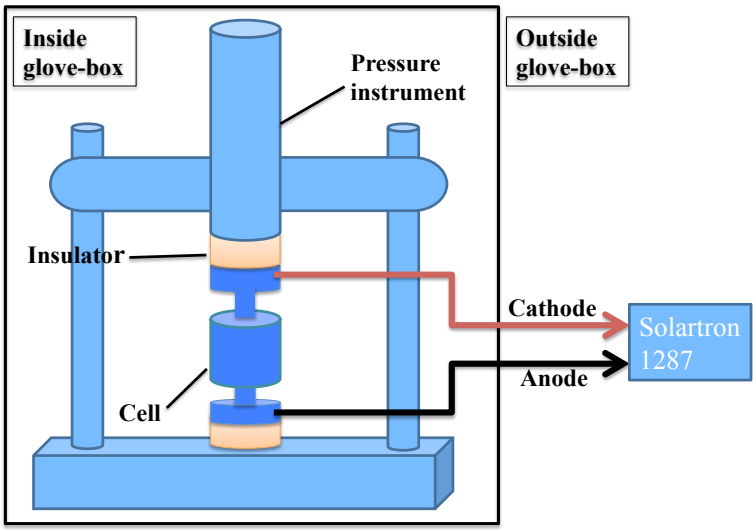

Figure 8. Schematic of maintaining the cell under pressure using the pressure instrument during the charge-discharge operation.

It is assumed that the properties of electrode-material system are virtually time-invariant, and it is one of the basic purpose in EIS to determine these properties, their interrelations, and their dependences on such controllable variables such as temperature, oxygen partial pressure, applied hydrostatic

pressure, and applied static voltage to the interface and measuring the phase shift and amplitude, of the resulting current at the same frequency. For example, any intrinsic property which influences the conductivity of an electrode-materials system can be studies by EIS. Also, the advantages of EIS measurements over other techniques are as follows:

- Rapid data acquisition
- Non-destructiveness
- High adaptability to a wide variety of different applications

The parameters derived from an EIS spectrum are generally classified into two categories: (i) those pertinent only to the material itself, such as conductivity, dielectric constant, mobilities of charges, equibrium concentrations of the charged species, and bulk generation-recombination rates; and (ii) those pertinent to an electrode-material

interface, such as adsorption-reaction rate constants, capacitance of the interdace region, and diffusion coefficient of neutral species in the electrode itself.

For most solid electrolytes, EIS measurements to evaluate the electrochemical behaviors of electrolytes and/or electrodes are usually made with cells which have two identical electrodes applied to the faces of a sample in the form of a circular cylinder of rectangular parallelepiped. In this study, the ionic conductivity of the samples was measured by ac impedance methods. The AC impedance methods is a method consisting of separating the bulk, grain boundary, and electrode components of the measured sample, and then calculating the essential bulk resistance-value by applying an ac voltage with a frequency change during the measurements. Also, the AC method is hardly affected by the polarization and the interfacial reaction between the electrolyte and electrode, which may arise by applying a dc voltage. However, EIS measurement system is a black box, and there are two serious problems, how to combine various equivalent circuits and how to interpret such data. When combining the equivalent circuits, there are three typical circuit elements, which show different responses to an ac signal. These circuit elements are usually regarded as a resistor, a capacitor, and an inductor, and their electrical properties are also called resistance, *R*, capacitance, *C*, and inductance, *L*, respectively as seen in Table 1.

Table 1. Electrical properties of typical circuit elements

Circuit element	*Resistance*	*Capacitor*	*Inductor*
Symbol, Unit	*R, Ω*	*C, F*	*L, H*
Phase shift	*0˚*	*–90˚*	*90˚*
Impedance	*ZR = R*	*ZC = (jwC)–1*	*ZL = jwL*

Furthermore, there exists a circuit element called Warburg impedance, Z_w besides these three ones.

$$Z_w = A_w w^{-1/2} (1-j) \quad [A_w: \text{Warburg coefficent}] \tag{2.7}$$

Warburg impedance shows the characteristic response which is caused by the diffusion process of the substance accompanying the electrode contribution, and the property in which the current is phase shifted -45º to the voltage with the magnitude proportional to $w^{-1/2}$.

In many cases, an equivalent circuit consisting of a simple RC element connected in parallel is used as shown in Figure 2.20. The complex impedance, Z* in Figure 2.20 is described by the following equation:

$$Z^* = \frac{R}{1+(\omega RC)^2} - jR\frac{\omega RC}{1+(\omega RC)^2} \tag{2.8}$$

where R: resistance, C: capacitance, w: angular frequency, j: imaginary number. ($j = (-1)^{1/2}$)

Above Eq. 2.8 consist of the real and imaginary components, for example, Z* = Z' - jZ", where Z' and Z" are the real and imaginary impedance components, respectively. Equation 2.8 may be transformed into:

$$\left(Z' - \frac{1}{2}R\right)^2 + Z''^2 = \frac{1}{4}R^2 \tag{2.9}$$

In Eq. 2.9, if the real part, Z' is plotted on the horizontal axis, and the imaginary part, Z" on the vertical axis, a graph called a "Nyquist plot" can be obtained. Figure 9 (a) shows the Nyquist plot for the circuit in Figure 9 (b). A semicircle which crosses at Z'-axis, 0, and R is observed. Consequently, the resistance-value is calculated from the diameter of the semicircle.

In this study, Electrochemical impedance spectroscopy (EIS) measurements of $LiNbO_3/LiCoO_2$/LGPS/$LiNbO_3/LiCoO_2$ and In-Li/LGPS/In-Li symmetric batteries were performed to confirm the characterized frequency of cathode/LGPS and anode/LGSP. EIS measurements of $LiNbO_3/LiCoO_2$/LGPS/In-Li batteries were

performed for batteries after the 10th and 20th discharging. All measurements used an impedance analyzer with an electrochemical interface (1260/1287, Solartron). The applied voltage during these trials was 10 mV and the frequency range was 0.1 to 10^5 Hz.

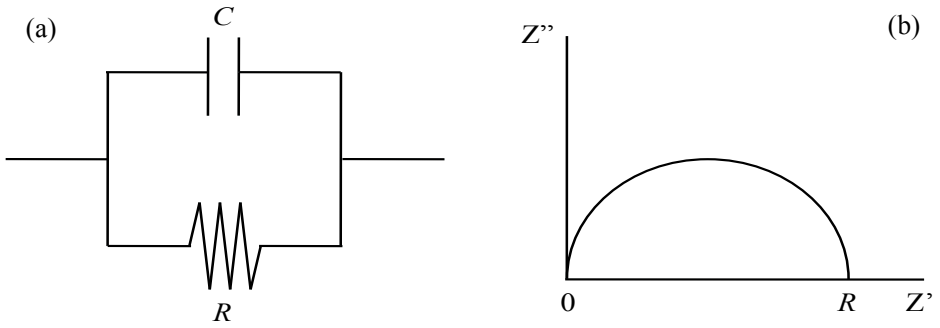

Figure 9. Simple circuit and Nyquist plot for simple.

References

[1] N. Kamaya, K. Homma, Y. Yamakawa, M. Yonemura, T. Kamiyama, Y. Kato, S. Hama, K. Kawamoto, A. Mitsui, Masaaki Hirayama, Ryoji Kanno, *Nature. Mater.*, 10 (2011) 682.

[2] N. Ohta, K. Takada, I. Sakaguchi, L. Zhang, R. Ma, K. Fukuda, M. Osada, T. Sasaki, *Electrochem. Commun*, 9 (2007) 1486.

[3] A. Sakuda, A. Hayashi, M. Tatsumisago, *Chem. Mater*, 22 (2010) 949.

[4] K. Takada, N. Ohta, L.Q. Zhang, K. Fukuda, I. Sakaguchi, R.Z. Ma, M. Osada, T. Sasaki, *Solid State Ionics*, 179 (2008) 1333.

[5] R.E. Wolf, *Research Chemist.*, USGS/CICT, 2005.

Chapter 3

Fabrication and electrochemical properties of $LiCoO_2$ and $Li_{10}GeP_2S_{12}$ composite electrode for use in all-solid-state batteries

3.1 Introduction

All solid-state lithium batteries show significant promise in large-scale applications such as plug-in hybrid electric vehicles and purely electric vehicles due to their inherent safety and high volumetric energy density [1-3]. However, the power density of these batteries, which is generally much lower than that of conventional lithium-ion batteries, must be addressed to allow their widespread use. The main rate determining step in all-solid-state batteries is the diffusion of lithium in the solid electrolytes since the lithium ion conductivity in such materials is low compared to that in liquid organic electrolytes, and this limits both the capacity and current density of the associated charge/discharge reactions [4-6]. Recently, it has been reported that a new sulfides solid electrolyte, $Li_{10}GeP_2S_{12}$ (LGPS), exhibits an extremely high lithium ionic conductivity of 12 mS cm^{-1} at room temperature, a value that exceeds even those of the organic electrolytes [10-14]. All solid-state batteries with LGPS electrolytes therefore allow for possible improvements in power density [15]. Another rate determining step in these devices is the lithium diffusion at the point of contact interface between the electrode and electrolyte particles since a small contact area will reduce the reaction rate at the interface. For this reason, the positive electrodes in these devices are compared of an active material together with a solid electrolyte so as to increase the contact area. Hence, the fabrication process of such composite electrodes should be investigated with the aim of obtaining a highly dispersed composite electrode exhibiting minimal aggregation [6-9,

[15-17]. However, there have been few reports investigating all solid-state batteries incorporating LGPS electrolytes, so little is known about the key factors associated with the fabrication process that may be able to improve the battery performance.

This part reports the effects of the $LiCoO_2$ and LGPS mixing conditions on the charge/discharge properties of a $LiCoO_2$/LGPS composite cathode/LGPS solid electrolyte/In-Li anode cell. The composite electrodes in this study were fabricated using a mill pot rotator, applying various rotation rates. The morphologies of the composite cathodes were investigated by scanning electron microscopy (SEM), and electrochemical charge/discharge and ac impedance measurements were performed to determine the interfacial resistance between the composite electrode and the electrolyte. The key factors involved with developing an all solid-state battery showing a high discharge capacity are discussed based on the mixing conditions and resulting electrochemical performances of the $LiCoO_2$/LGPS composite cathodes.

3.2 Sample characterization

Figure 1 shows SEM images and XRD patterns of $LiCoO_2$ powders before and after spray coating with $LiNbO_3$. Whereas the pristine $LiCoO_2$ powder and very flat surfaces and sharp particle edges (Figure 1a), the spray-coated $LiCoO_2$ powder exhibited rounded edges (Figure 1b). The XRD patterns showed no changes in the peak positions and intensities after the coating process (Figure 1c, d), confirming that no chemical reaction occurred between the $LiCoO_2$ and the $LiNbO_3$ during the coating and annealing processed. Table 1 summarizes the weight ratios of the $LiNbO_3$ layer to the $LiCoO_2$ and the average thicknesses of the $LiNbO_3$ layers. The $LiNbO_3$ weight ratios in the products were determined by ICP analyses and the average coating thicknesses were calculated using the weight ratio in the product and the surface area (0.23 m^2 g^{-1}) together with the weight of the $LiCoO_2$ powder (500 g) employed during spray coating. As the spray coating during increased, the $LiNbO_3$ weight ratios were gradually reduced below the starting values. In this study, we obtained $LiNbO_3$-coated $LiCoO_2$ with weight ratios

ranging from 0.12 to 1.76 wt.%.

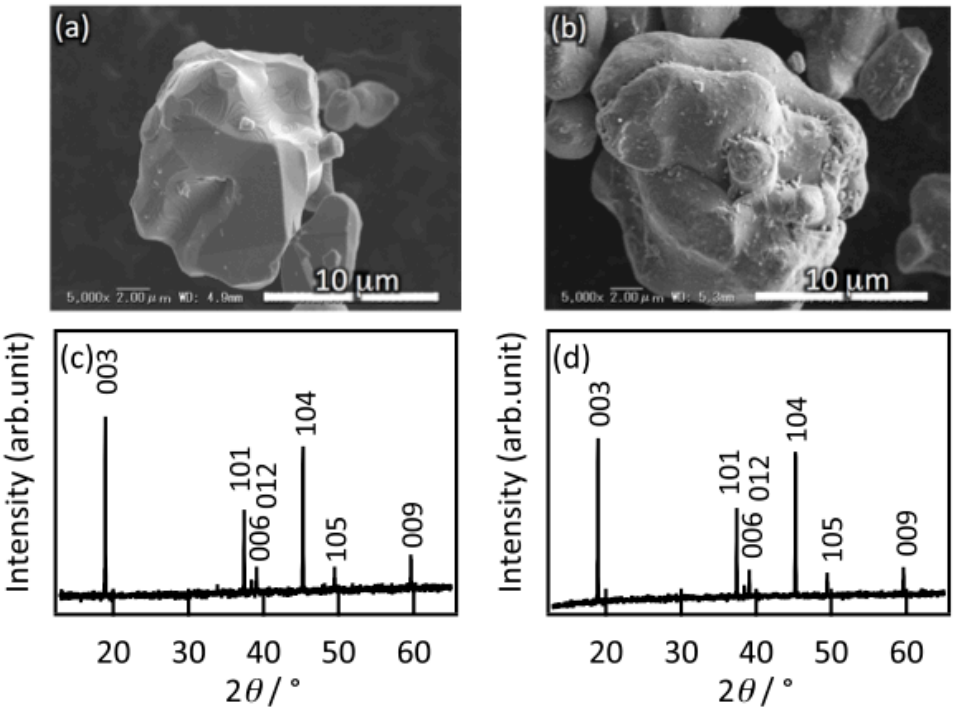

Figure 1. SEM images and XRD patterns for uncoated $LiCoO_2$ (a,c) and $LiNbO_3$ coated $LiCoO_2$ (b, d). The weight ratio of $LiNbO_3$ to $LiCoO_2$ was 0.12 wt.% in the starting solution.

Table 1. Fractions of $LiNbO_3$ in starting materials and products and average layer thicknesses.

Fraction of $LiNbO_3$ in starting material (wt.%)	0.11	0.59	1.34	2.49
Fraction of $LiNbO_3$ in product (wt.%)	0.12	0.48	1.16	1.76
Average thickness of $LiNbO_3$ on $LiCoO_2$ particles (nm)	1.0	4.8	11.4	17.4

3.3 Electrochemical properties

A 1.76 wt.% $LiNbO_3$-coated $LiCoO_2$ sample was used to investigate the effects of mixing conditions when combining this material with the LGPS electrolyte to fabricate the composite positive electrodes. Figure 2 shows a schematic of the mixing process using a mill pot rotator, along with SEM images of the $LiCoO_2$/LGPS composites ground for 30 min at different rotation rates. Small LGPS particles are seen to have been dispersed on each $LiCoO_2$ particle in the composite ground at 140 rpm (Figure 2b). In contrast, some LGPS aggregates are observed on the composites as the rotation rate is increased (Figure 2 c,d). Thus mild mixing with a low rotation rate of 140 rpm generated well-dispersed composite electrodes. Figure 3a shows the first charge-discharge curves obtained from 1.76 wt.% $LiNbO_3$-coated $LiCoO_2$/LGPS composite positive electrodes fabricated at different rotation rates. A plateau was observed in the vicinity of 3.4 V (vs. In-Li anode) in these curves, corresponding to reversible lithium (de)intercalation into the $LiCoO_2$. The composite ground at 140 rpm exhibited a first discharge capacity of 105 mAh g^{-1}, which the first discharge capacities decreased to 99 and 71 mAh g^{-1} for the composites ground at 250 and 350 rpm, respectively. The well-dispersed composite electrodes could have had a greater contact area between the $LiCoO_2$ and LGPS, which would serve to increase the utilization efficiency of the $LiCoO_2$ active material in the composite electrode. Effects of the grinding time on the charge/discharge capacity were investigated at a fixed rotation rate of 140 rpm (Figure 3b). The first discharge capacity increased from 65 to 108 mAh g^{-1} when the grinding time was increase from 10 to 20 min, and thus a short time grinding under the mild conditions led to insufficient mixing. No significant change in the capacity was observed when increasing the grinding time from 20 to 30 min. Longer mixing times over 20 min with low grinding energy gave better mixing of the $LiCoO_2$ and LGPS with no LGPS aggregation.

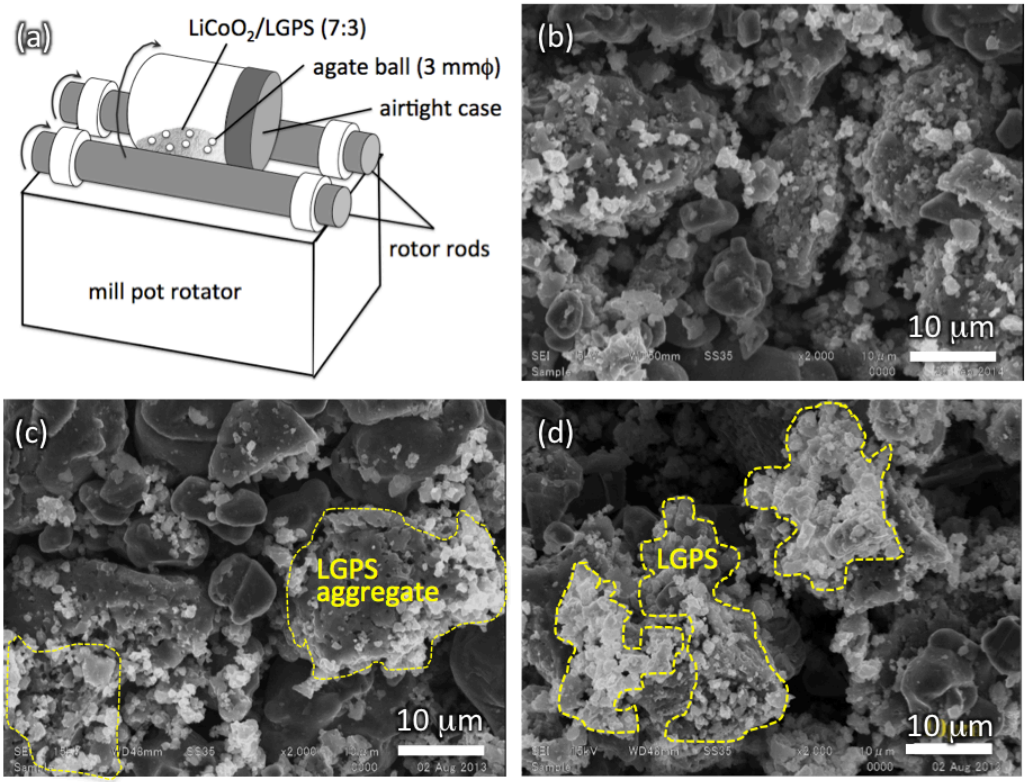

Figure 2. (a) Schematic of mixing process of $LiCoO_2$ and LGPS using a mill pot rotator and SEM miages of 1.76 wt.% $LiNbO_3$-coated $LiCoO_2$/LGPS mixtures ground under different rotating rates of (b) 140 rpm, (c) 250 rpm, and (d) 350 rpm. The ground time was 30 min. Large particles with dark gray color and small particles with white gray color in Fig. (b-d) correspond to $LiCoO_2$ and $Li_{10}GeP_2S_{12}$, respectively.

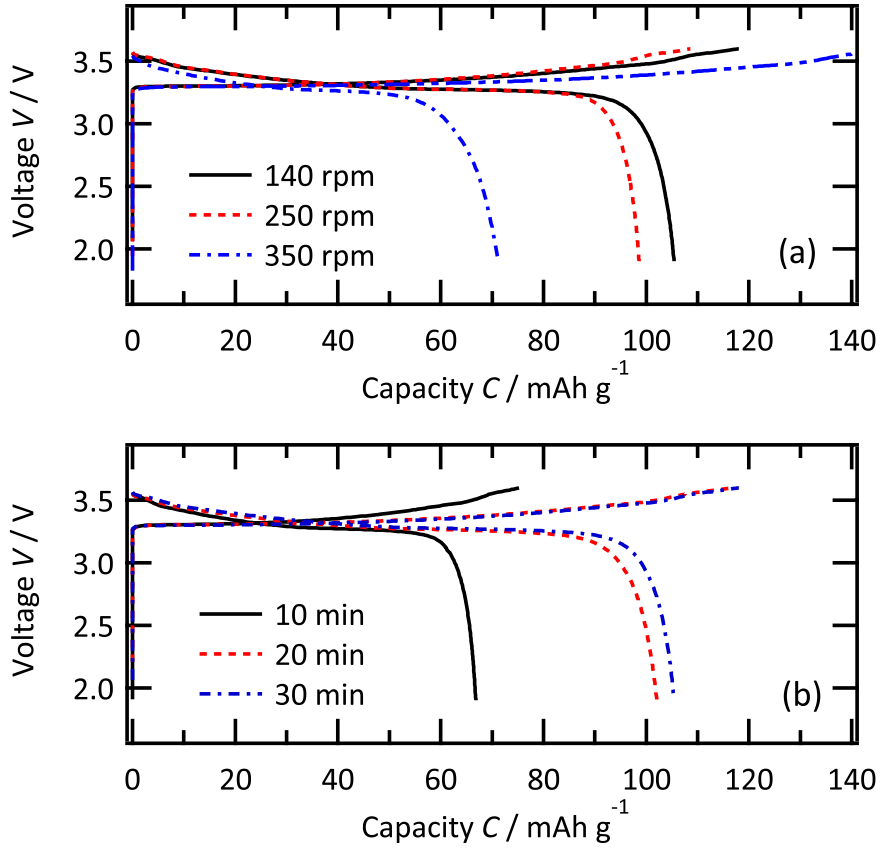

Figure 3. The first charge/discharge curves of 1.76 wt.% $LiNbO_3$-coated $LiCoO_2$/LGPS composite electrodes fabricated (a) by grinding for 30 min at rotating rates of 140 rpm, 250 rpm, and 350 rpm and (b) by grinding for 10, 20, and 30 min at the rotating rates of 140 rpm. The constant current density used was 7 mA g^{-1}.

The allow fabrication of the $LiNbO_3$/$LiCoO_2$/LGPS composites under optimal mixing conditions, the LGPS was ground to reduce the particle size before mixing with the $LiNbO_3$/$LiCoO_2$. Figure 4 presents SEM images of LGPS powders ground for different time spans and the first charge/discharge curves of the $LiCoO_2$/LGPS composite electrode fabricated using each LGPS powder. The LGPS powder ground 5 min (LGPS5) consisted of primary particles with particles sizes over 5 μm as well as micro-sized aggregates of these nanosized primary particles. The $LiCoO_2$/LGPS composite electrode showed a low discharge capacity of 87 mAh g^{-1} compared to the theoretical capacity of 125 mAh g^{-1} when the $LiCoO_2$ cathode is charged to 4.2 V vs. Li/Li^+ [18]. This result indicated insufficient dispersion of the LGPS, generating a reduced contact area with the $LiCoO_2$ due to the large sizes of the primary particles and the aggregates. The LGPS powder ground for 10 min (LGPS10) consisted of small particles less than 2 μm in size, and no severe aggregation was observed. The discharge capacity of the $LiCoO_2$/LGPS10 increased to 124 mAh g^{-1}, corresponding to the theoretical capacity. Thus the use of small LGPS particles with no aggregation let to a highly-dispersed composite electrode with a large contact area between the $LiCoO_2$ with LGPS. The particle size gradually decrease with increasing grinding time from 10 min through 30 to 120 min, although aggregates of the small LGPS particles increased at longer grinding times. The discharge capacities of the $LiCoO_2$/LGPS30 and $LiCoO_2$/LGPS120 devices were 104 and 102 mAh g^{-1}, respectively. Thus prolonged grinding of the LGPS could not improve the utilization efficiency of the $LiCoO_2$ active material. This result indicated that the aggregation of LGPS had a greater impact than the particle size with regard to the fabrication of $LiCoO_2$/LGPS composites with high electrochemical reactivity.

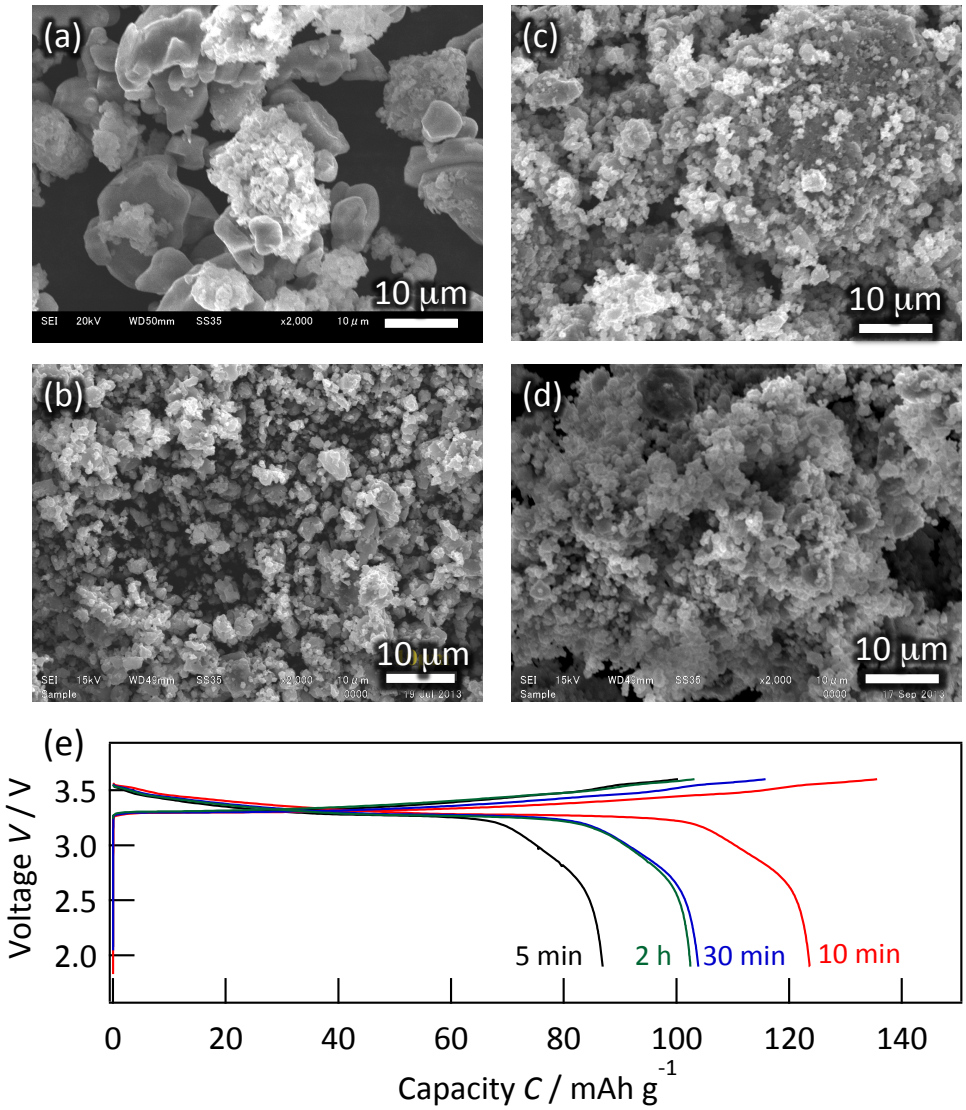

Figure 4. SEM images of LGPS powders pre-ground in a mortar of different times of (a) 5 min, (b) 10 min, (c) 30 min, and (d) 120 min, (e) the first charge/discharge curve of 0.48 wt.% $LiNbO_3$-coated $LiCoO_2$/LGPS composite electrodes using each LGPS powder. The composites were fabricated at a rotating rate of 140 rpm for 30 min. The constant current density used was 7 mA g^{-1}.

3.4 Effect of coating thickness

Figure 5a-d shows the charge/discharge curves obtained from $LiCoO_2$/LGPS10 composite electrodes using $LiCoO_2$ coated with $LiNbO_3$, applying varying weight ratios between the $LiNbO_3$ and $LiCoO_2$ of 0.12, 0.48, 1.16 and 1.76 wt.%. The rotation rate and grinding time for mixing were fixed at 140 rpm and 30 min, respectively. The uncoated $LiCoO_2$ electrode exhibited no reversible capacity (see Supporting Information), while charge/discharge reactions were observed with the composite electrode incorporating the 0.12 wt.%-$LiNbO_3$ coated $LiCoO_2$. It has been proposed that a high resistance layer is formed by ionic diffusion from a sulfide electrolyte to $LiCoO_2$ due to large difference in electrochemical potentials of Li between the sulfide and the oxide [6,7,19]. The $LiNbO_3$ coating, however, suppresses the interfacial layer formation, leading to reduce reaction resistance. Similar to previous reports regarding other sulfide electrolytes, an interfacial layer with a high resistance was formed between the $LiCoO_2$ and LGPS electrolyte, but this resistance was decrease by the application of the $LiNbO_3$ layer. The discharge capacity of the 0.12 wt.%-$LiNbO_3$/$LiCoO_2$ specimen increased from 35 to 74 mAh g^{-1} from the first to 20th cycle with decreasing over voltages. Compared to this, weight ratio of 0.48, 1.16 and 1.76 wt.% $LiNbO_3$ to $LiCoO_2$ showed much higher discharge capacities of 124, 97 and 95 mAh g^{-1} at the first cycle. Furthermore, the over voltages of the 0.48, 1.16 and 1.76 wt.% $LiNbO_3$/$LiCoO_2$ were much smaller than that of the 0.12 wt.% $LiNbO_3$/$LiCoO_2$. These results confirmed that the interfacial resistance could be changed by varying the thickness of the coating layer. Figure 5e summarized the variations in the first discharge capacities of $LiNbO_3$/$LiCoO_2$/LGPS composite electrodes with varying amounts of the $LiNbO_3$ coating layer.

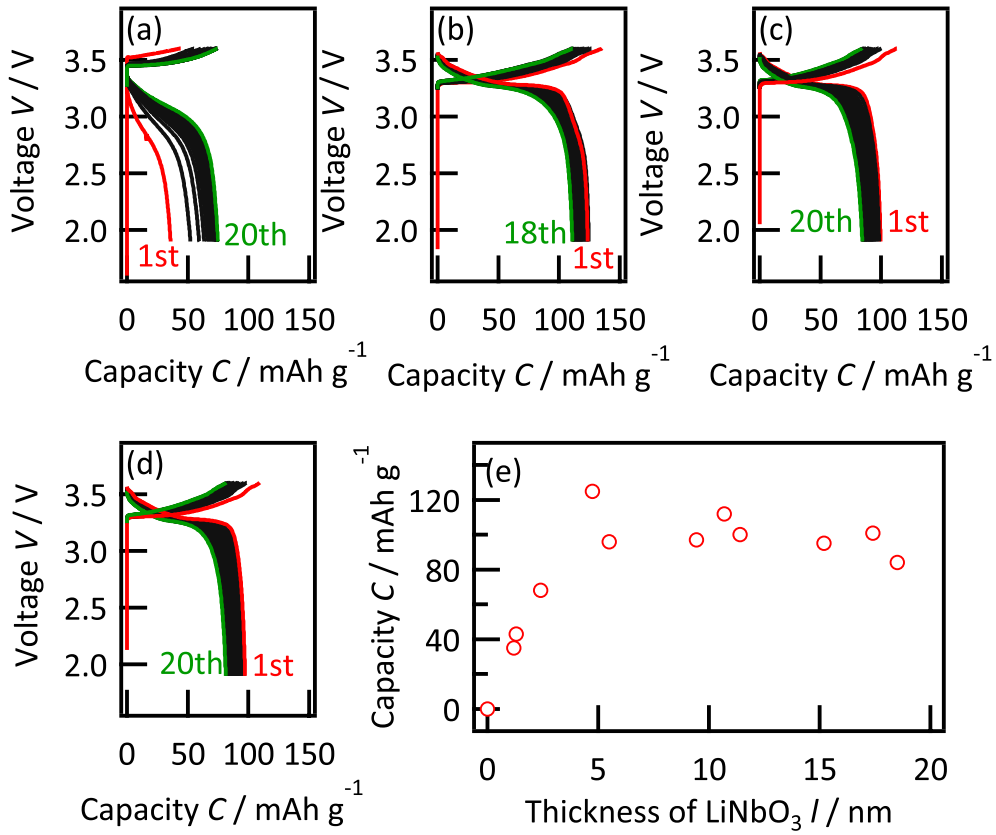

Figure 5. (a-d) Charge/discharge curves of $LiNbO_3$-coated $LiCoO_2$/LGPS composite electrodes fabricated at a rotating rate of 140 rpm for 30 min. Weight ratios of $LiNbO_3$ to $LiCoO_2$ were (a) 0.12 wt.%, (b) 0.48 wt.%, (c) 1.16 wt.% and (d) 1.76 wt.%. The constant current density used was 7 mA g^{-1}. (e) Variation of the first discharge capacity with calculated thickness of $LiNbO_3$ coating.

3.5 Interfacial resistance

The origin of the capacity fading of the $LiNbO_3$/$LiCoO_2$/LGPS composite electrodes was investigated using EIS analyses. Figure 6a,b show Nyquist plots of the electrochemical impedances of an all-solid-state battery composed of $LiNbO_3$ (0.48 wt.%)-$LiCoO_2$/LGPS/In-Li after the 10th and 20th discharges. Two semicircles observed at approximately 500 and 1 Hz. The electrochemical impedance spectra of $LiNbO_3$/$LiCoO_2$/LGPS/$LiNbO_3$/$LiCoO_2$ and In-Li/LGPS/In-Li symmetric cells exhibited a semicircle with a characteristic frequency of 500 and 1.5 Hz, respectively, shown in Figure 6c, d. Hence, the diameters of the semicircles observed in the vicinity of 500 and 1 Hz for each cell attributed to the interfacial resistances between the $LiNbO_3$/$LiCoO_2$ cathode (R_c) and the LGPS electrolyte and between the In-Li anode and the LGPS electrolyte (R_a), respectively. These characteristic frequency values are similar to those of the interfaces of $LiCoO_2$ and In-Li with other sulfide electrolytes [2,17]. The R_a value increased from 690 Ω at the 10th discharge to 2420 Ω at the 20th discharge. In contrast, no significant increase in the R_c value was observed from the 10th discharge (280 Ω) to the 20th discharge (290 Ω). This result indicates that the capacity fading of the $LiNbO_3$/$LiCoO_2$/LGPS interface. A first principles calculation suggests that the LGPS is unstable at low electrochemical potential of Li and is decomposed to another phase [20]. An interfacial layer with a high resistance could thus be formed at the In-Li/LGPS interface due to the LGPS decomposition induced by the contact with the In-Li anode (at about 0.6 V vs. Li/Li^+) [21]. The In-Li/LGPS interface should thus also be modified to improve the cycling stability of $LiNbO_3$/$LiCoO_2$/LGPS/In-Li batteries.

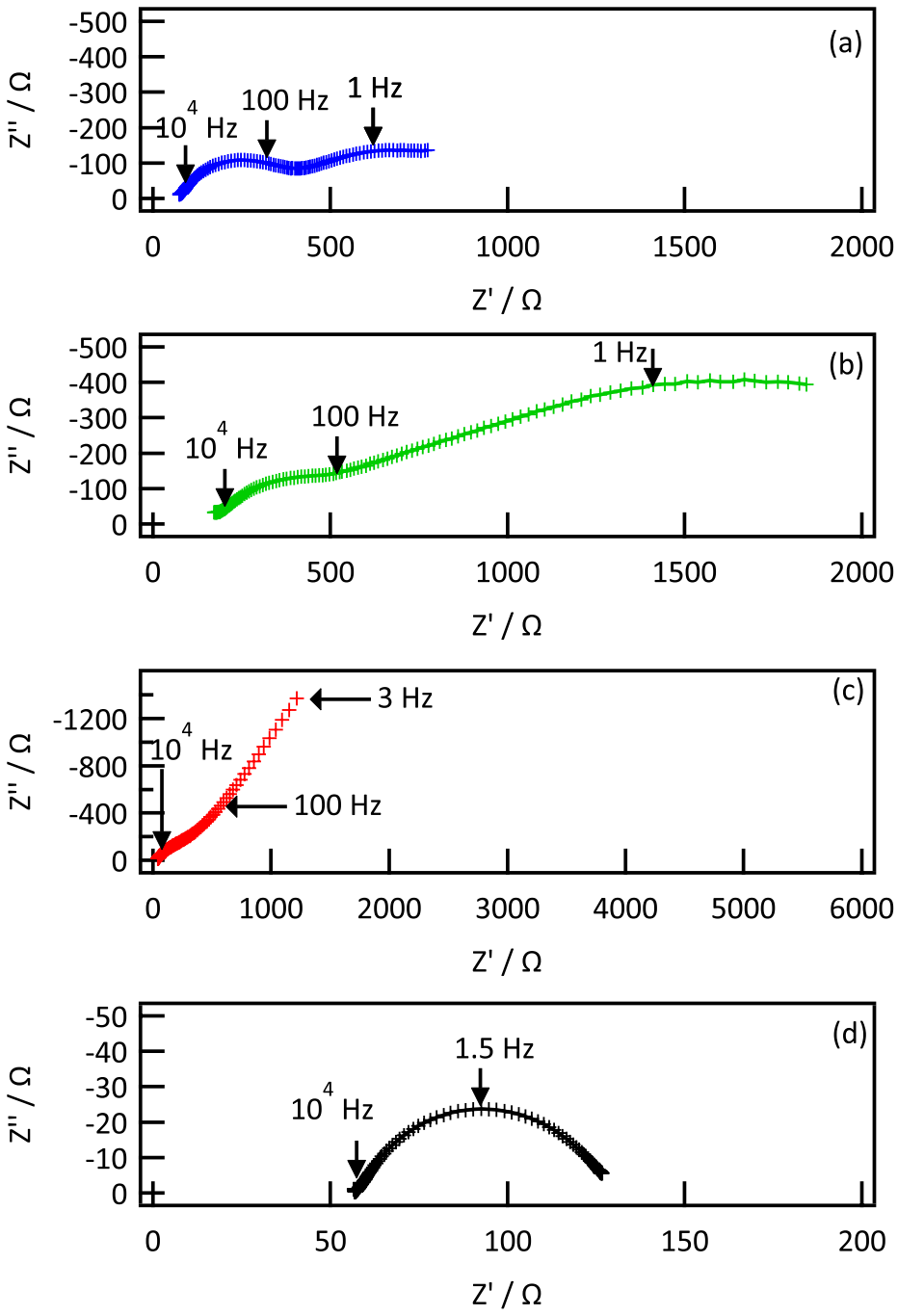

Figure 6. Electrochemical impedance spectra of $LiNbO_3$(0.48 wt.%)/$LiCoO_2$/LGPS/In-Li cell after (a) tenth and (b) twentieth discharging and of (c) $LiNbO_3$-$LiCoO_2$/LGPS/$LiNbO_3$-$LiCoO_2$ and (d) In-Li/LGPS/In-Li symmetric cells.

3.6. Conclusion

A composite cathode consisting of a $LiNbO_3$-coated $LiCoO_2$ active material and a LGPS super lithium ionic conductor was fabricated under various conditions to clarify the key parameters associated with the improvement of the reaction efficiency of $LiNbO_3$/$LiCoO_2$/LGPS/In-Li cells. The effects of the fabrication process on the charge/discharge capacity of the batteries may be summarized as follows.

(1) The LGPS particles readily aggregate during the mixing process. Highly dispersed composites were successfully obtained by mild grinding applying a mill pot rotation rate of 140 rpm for 30 min with 3 mmϕ agate balls.

(2) The weight ratio of the $LiNbO_3$ layer to the $LiCoO_2$ affects the resistance at the $LiCoO_2$/LGPS interface. The weight ratio should be over 0.5 wt.% to decrease the interfacial resistance.

(3) The first discharge capacity of the composite electrode fabricated with the optimized conditions was 124 mAh g^{-1} when operating at a current density of 7 mA g^{-1}.

(4) The capacity fading observed for the cell using the $LiNbO_3$/$LiCoO_2$/LGPS composite cathode was primarily caused by the increase in the resistance to lithium diffusion at the In-Li anode/the LGPS electrolyte interface.

References

[1] B. Key, R. Bhattacharyya, M. Morcrette, V. Seznec, J.M. Tarascon, C.P. Grey, *J. Am. Chem. Soc.,* 131(2009) 9239.

[2] A. Sakuda, A. Hayashi, M. Tatsumisago, *Chem. Mater.,* 22 (2010) 949.

[3] T. Inada, T. Kobayashi, N. Sonoyama, A. Yamada, S. Kondo, M. Nagao, R. Kanno, *J. Power Sources.* 194 (2009) 1085

[4] R. Kanno, M, Murayama, *J. Electrochem. Soc.*, 148 (2001) A742.

[5] F. Mizuno, A. Hayashi, K. Tadanaga, M. Tatsumisago, *Adv. Mater.*, 17 (2005) 918.

[6] N. Ohta, K. Takada, L.Q. Zhang, R.Z. Ma, M. Osada, T. Sasaki, *Adv. Mater.*, 18 (2006), 2226.

[7] N. Ohta, K. Takada, I. Sakaguchi, L.Q. Zhang, R.Z. Ma, K. Fukuda, M. Osada, T. Sasaki, *Electrochem Commun.*, 9 (2007) 1486.

[8] K. Takada, N. Ohta, L.Q. Zhang, K. Fukuda, I. Sakaguchi, R.Z. Ma, M. Osada, T. Sasaki, *Solid State Ionics*, 179 (2008) 1333.

[9] H. Kitaura, A. Hayashi, K. Tadanaga, M. Tatsumisago, *Solid State Ionics*, 192 (2011) 304.

[10] N. Kamaya, K. Homma, Y. Yamakawa, M. Yonemura, T. Kamiyama, Y. Kato, S. Hama, K. Kawamoto, A. Mitsui, Masaaki Hirayama, Ryoji Kanno, *Nat. Mater.*, 10 (2011) 682.

[11] Inaguma, Y. et al. High ionic-conductivity in lithium lanthanum titanate. *Solid State Commun.*, 86 (1993) 689.

[12] A. Hayashi, K. Minami, F. Mizuno, M. Tatsumisago, *J. Mater. Sci.*, 43 (2008) 1885.

[13] S. Kondo, K. Takada, Y. Yamamura, *Solid State Ionics,* 53 (1992) 1183.

[14] K. Takada, N. Aotani, S. Kondo, *J. Powder Sources*, 43 (1993) 135.

[15] Y. Kato, K. Kawamoto, R. Kanno, M. Hirayama, *Electrochemistry*, 80 (2012) 749.

[16] A. Sakuda, A. Hayashi, T. Ohtamo, S. Hama. M. Tatsumisago, *J. Power Sources*, 196 (2011) 6735.

[17] A. Sakuda, H. Kitaura, A. Hayashi, K. Tadanaga, M. Tatsumisago, *J. Electrochem. Soc.*, 156 (2009) A27.

[18] T. Ohzuku and A. Ueda, *J. Electrochem. Soc.*, 141 (1994) 2972.

[19] K. Takada, N. Ohta, L. Zhang, X. Xu, B. T. Hang, T. Ohnishi, M. Osada, T. Sasaki. *Solid State Ionics*, 225 (2012) 594.

[20] Y. Mo, S. P. Ong, and G. Ceder, *Chem. Mater.*, 24 (2012) 15.

[21] T. Kobayashi, A. Yamada, and R. Kanno, *Electrochim. Acta*, 53 (2008) 5045.

Chapter 4

Fabrication and all solid-state battery performance of $TiS_2/Li_{10}GeP_2S_{12}$ composite electrodes

4.1 Introduction

The use of solid in place of liquid electrolytes in lithium-ion batteries has greatly improved reliability owing to the greater range of safe operating temperatures of all-solid-state batteries [1-3]. However, low ionic conductivity of solid electrolytes compared to liquid electrolytes is a major technical issue for their practical use. During these 15 years, lithium ion conductors having high conductivity have been developed as a solid electrolyte [4-8]. Among them, a lithium germanium phosphosulfide $Li_{10}GeP_2S_{12}$ exhibits an extremely high lithium ion conductivity of 12 mS cm^{-1} at room temperature, which exceeds even that of organic liquid electrolytes [7]. Recently, some reports have demonstrated successful operation of all-solid-state batteries with the $Li_{10}GeP_2S_{12}$–type electrolytes and oxide cathode materials such as $LiCoO_2$ [7,9], $LiNi_{1/3}Mn_{1/3}Co_{1/3}O_2$ [10], $LiNi_{0.8}Co_{0.15}Al_{0.05}O_2$ [11]. However, the oxide cathode-solid electrolyte interfaces exhibit a highly-resistive interfacial layer for lithium diffusion due to formation of lithium-depleted space-charge layer [12] and/or mutual diffusion of cation species [13], thus giving a very low capacity for solid-state batteries. Although surface coating on cathode materials by lithium-ion conductive oxides is an efficient way to decrease the interfacial resistance [13-14], it could take a cost to fabricate a uniform coating [15]. When there is no observable resistance between the sulfide cathode and sulfide electrolyte, it is not necessary to modify the cathode [16-19]. However, to date, there have been few reports of solid-state batteries comprising a sulfide cathode and $Li_{10}GeP_2S_{12}$ electrolytes

[19], and the cell cycling characteristics remain unclear.

In this chapter, TiS_2 with a layered structure has been focused on as the cathode. TiS_2 has a hexagonal close-packed structure where each Ti is surrounded by six S in an octahedral structure. TiS_6 octahedra shared the edges to form a layered structure [20]. Li can intercalate into possible spaces between the TiS_6 layers [20]. The electrochemical reaction is as follows: $TiS_2 + Li^+ + e^- \rightleftarrows LiTiS_2$; moreover, the theoretical capacity is 239 mAh g^{-1}. This capacity is much higher than that of conventional $LiCoO_2$ used as a cathode for all solid-state batteries (130 mAh g^{-1}). Jung *et al.* has reported a TiS_2 cathode and $Li_{10}GeP_2S_{12}$ electrolyte solid-state battery having a capacity 200 mAh g^{-1} [19]. When Li intercalates into all possible spaces in TiS_2, the volume of TiS_2 layer expands by approximately about 12 % [21]. The TiS_2 composite cathode comprises the TiS_2 active material and $Li_{10}GeP_2S_{12}$ electrolyte, and contact between the bulk grains is very important. The large volume change of Li_xTiS_2 during charge-discharge cycles could lead to the decrease in the physical contact between the TiS_2 and the $Li_{10}GeP_2S_{12}$ electrolyte. However, the physical contact and the related cycle stability of the $TiS_2/Li_{10}GeP_2S_{12}$ composite electrodes have not been clarified. Here, all solid-state batteries with the $TiS_2/Li_{10}GeP_2S_{12}$ composite cathode were fabricated, and their electrochemical properties were characterized. Furthermore, effects of applied pressure during charge-discharge cycles were investigated to improve the cycle stability and the rate capability.

4.2 Characterization of $TiS_2/Li_{10}GeP_2S_{12}$ composite

Figure 1 shows the XRD patterns and SEM images of TiS_2 before and after grinding with ball milling. Before ball milling, the TiS_2 powder showed a layer structure (*P*-3*m*1), with the lattice parameters a = 3.4079(3) Å and c = 5.6989(6) Å. Whereas, no changes in the peak position were observed after ball milling, the diffraction peaks became broader and their intensity decreased. This indicates that the average size of the TiS_2 particles decreased after ball milling. SEM images from before and after ball milling

showed that the average size of TiS_2 particles reduced from 1-2 μm to 200-500 nm. Using BET measurements, it was observed that the surface area of TiS_2 increased from 3.2 $m^2 g^{-1}$ to approximately 45.6 $m^2 g^{-1}$ after ball milling.

Figure 2 shows the SEM images of $TiS_2/Li_{10}GeP_2S_{12}$ (3:7 wt.%) composite cathodes ground for 2, 5 and 10 min using the Vortex mill. Many aggregations of TiS_2 are observed for the $TiS_2/Li_{10}GeP_2S_{12}$ ground for 2 min, which means that TiS_2 could not disperse around $Li_{10}GeP_2S_{12}$ well. The mixing condition became better as the grinding duration increased. Figure 3 shows the charge-discharge curves of the $TiS_2/Li_{10}GeP_2S_{12}$ ground for different durations. The batteries were fabricated using a compressive forming pressure of 19 MPa and were sealed into an unpressed cell. All samples showed reversible charge-discharge behavior between 2.0 V and 1.2 V *vs.* In-Li. It has been reported that the lithium intercalation into TiS_2 proceeds at around 2.1 V vs. Li/Li^+ [22]. Because the potential of the In-Li alloy is about 0.6 V higher than that of Li/Li^+, the observed charge-discharge curves confirm the lithium (de)intercalation from/into the TiS_2 lattice. The first discharge capacity increased from 203 mAh g^{-1} to 239 mAh g^{-1} as the grinding duration increased from 2 min to 10 min. TiS_2 and $Li_{10}GeP_2S_{12}$ were well-dispersed in the 10 min-ground sample, resulting in the highest charge-discharge capacity. Thus, the duration was set to 10 min at the following experiments.

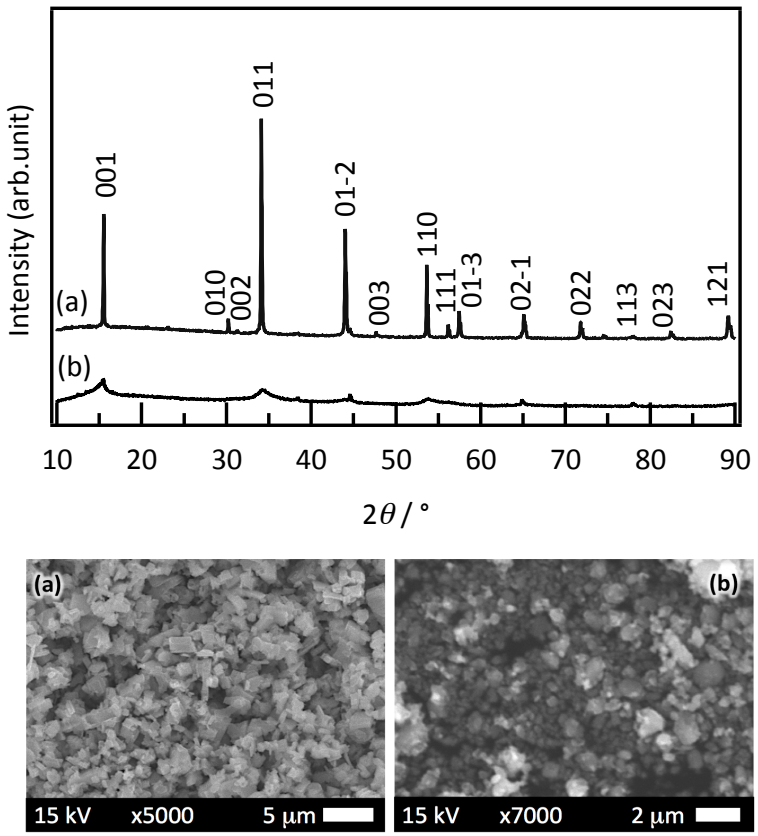

Figure 1. XRD patterns and SEM images of TiS_2 (a) before and (b) after grinding with ball milling.

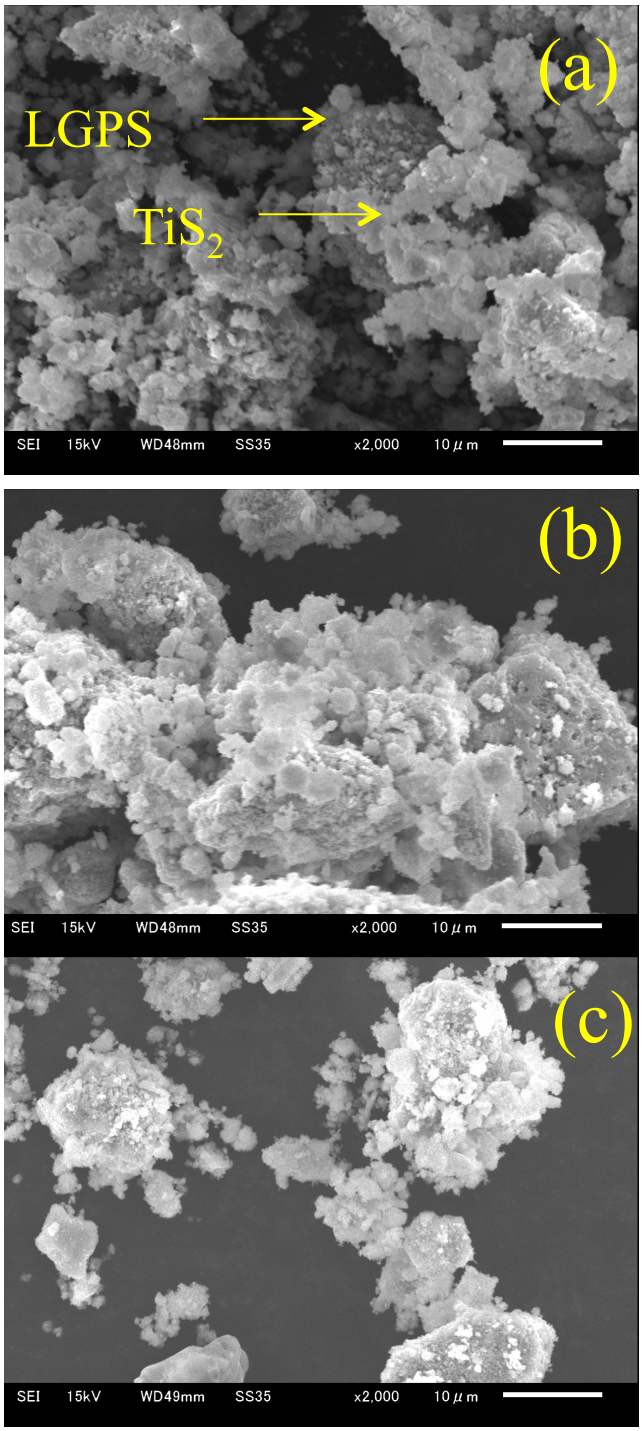

Figure 2. SEM images of $TiS_2/Li_{10}GeP_2S_{12}$ composite cathodes ground for (a) 2 min, (b) 5 min, and (c) 10 min.

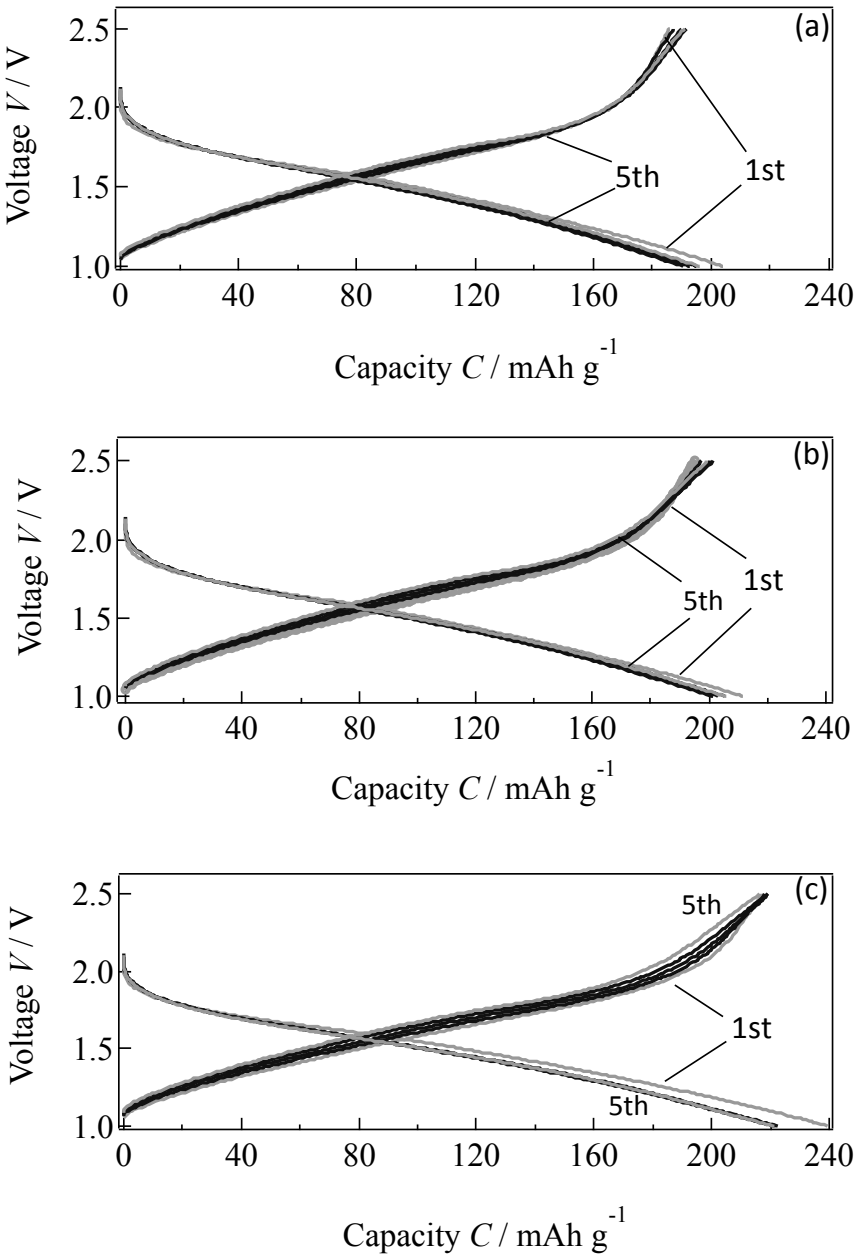

Figure 3. Charge-discharge curves of $TiS_2/Li_{10}GeP_2S_{12}$ composite cathodes ground for (a) 2 min, (b) 5 min, and (c) 10 min.

4.3 Effect of ionic conductivity of solid-electrolytes on battery performance

Electrochemical properties of TiS_2 was investigated with a different sulfide electrolyte $Li_{3.25}Ge_{0.25}P_{0.75}S_4$. Figure 4 shows the charge-discharge curves of an all solid-state battery of $TiS_2/Li_{3.25}Ge_{0.25}P_{0.75}S_4$/In-Li. The $TiS_2/Li_{3.25}Ge_{0.25}P_{0.75}S_4$ composite cathode was fabricated with the same conditions with the $TiS_2/Li_{10}GeP_2S_{12}$ (ground for 10 min). The first discharge and charge capacities were 216 and 185 mAh g^{-1}, which were smaller than those of $TiS_2/Li_{10}GeP_2S_{12}$/In-Li. The superior electrochemical properties of the battery with the $Li_{10}GeP_2S_{12}$ electrolyte could be associated with the higher ionic conductivity of 1.2 mS cm^{-1} than the $Li_{3.25}Ge_{0.25}P_{0.75}S_4$ (0.2 mS cm^{-1}). The highly ionic conduction could enhance the lithium diffusion at the solid-solid interface between the electrode and the solid-electrolyte.

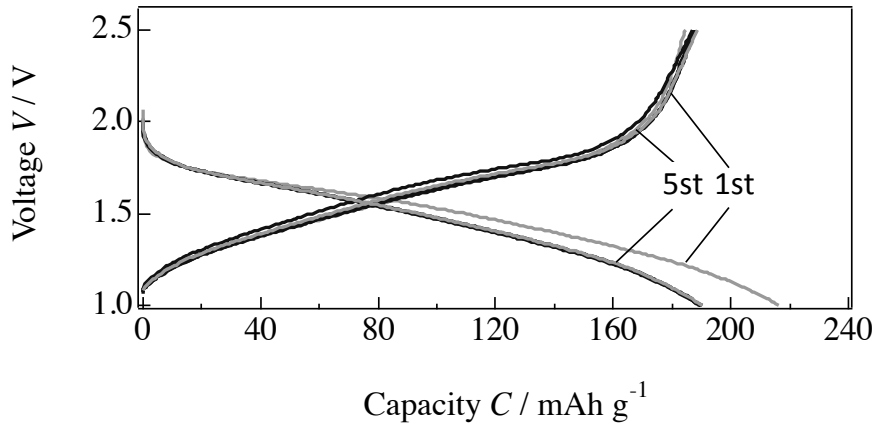

Figure. 4 Charge-discharge curves of $TiS_2/Li_{3.25}Ge_{0.25}P_{0.75}S_4$/In-Li at a current density of 0.044 mA cm^{-2}.

4.4 Cycle retention and rate capability of $TiS_2/Li_{10}GeP_2S_{12}$/In-Li

Figure 5 shows charge/discharge curves of $TiS_2/Li_{10}GeP_2S_{12}$/In-Li batteries under different current densities of 0.1, 0.2 and 1 C. At current density of 0.1 C, the first discharge and charge capacity were 206 and 185 mAh g^{-1}, respectively. Approximately

0.8 mol Li takes part in intercalation into the TiS_2 lattice, which are estimated from the observed capacities. The irreversible capacity of the first charge-discharge operation is about 21 mAh g^{-1}. A first principle calculation has shown that $Li_{10}GeP_2S_{12}$ is unstable below 2 V *vs.* Li / Li^+ and electrochemically decomposes to form a thin interfacial layer [23-24]. Thus, the irreversible capacity could be associated with the interfacial layer formation. The charge-discharge efficiency was approximately 100 % at the subsequent cycles. However, after the 5th cycle, the reversible capacity gradually decreased to 140 mAh g^{-1} by the 18th cycle. When the current density was 0.2 C, the performance of the initial five cycles was similar to that at a current rate of 0.1 C. The capacity decreased sharply to around 120 mAh g^{-1} by the 20th cycle, representing around a 60 % decrease. When the current densities were 1 C and 2 C, the charge-discharge capacities decreased obviously. Particularly at 2 C, the discharge-charge capacities decreased from 113 and 101 mAh g^{-1} to 79 and 78 mAh g^{-1}, respectively, from the first to fifth cycle. These results indicate that the capacity and cycle stability decrease as the current density increases.

During the lithium (de)intercalation, the host lattice is expanded and contracted repeatedly. When the volume changes are large, the contact between the solid electrolyte and conductive additive is disputed, reducing the electrochemically-active region. The lithiated $LiTiS_2$ phase has a considerably larger lattice volume (64.1 $Å^3$) than TiS_2 (57.1 $Å^3$), therefore, the severe capacity fading could be associated to decrease in the electrochemically active regions in the composite electrodes. In contrast, an all solid-state battery with a $LiCoO_2$/$Li_{10}GeP_2S_{12}$ composite electrode, which is fabricated using the same cell conditions, has exhibited excellent electrochemical performance, when Li intercalates to give $Li_{0.55}CoO_2$ [25]. In this case, the volume change is about 2 % of the $LiCoO_2$ host lattice. This result supports that the sharp volume changes have a more obvious effect on the cycle stability of all solid-state batteries.

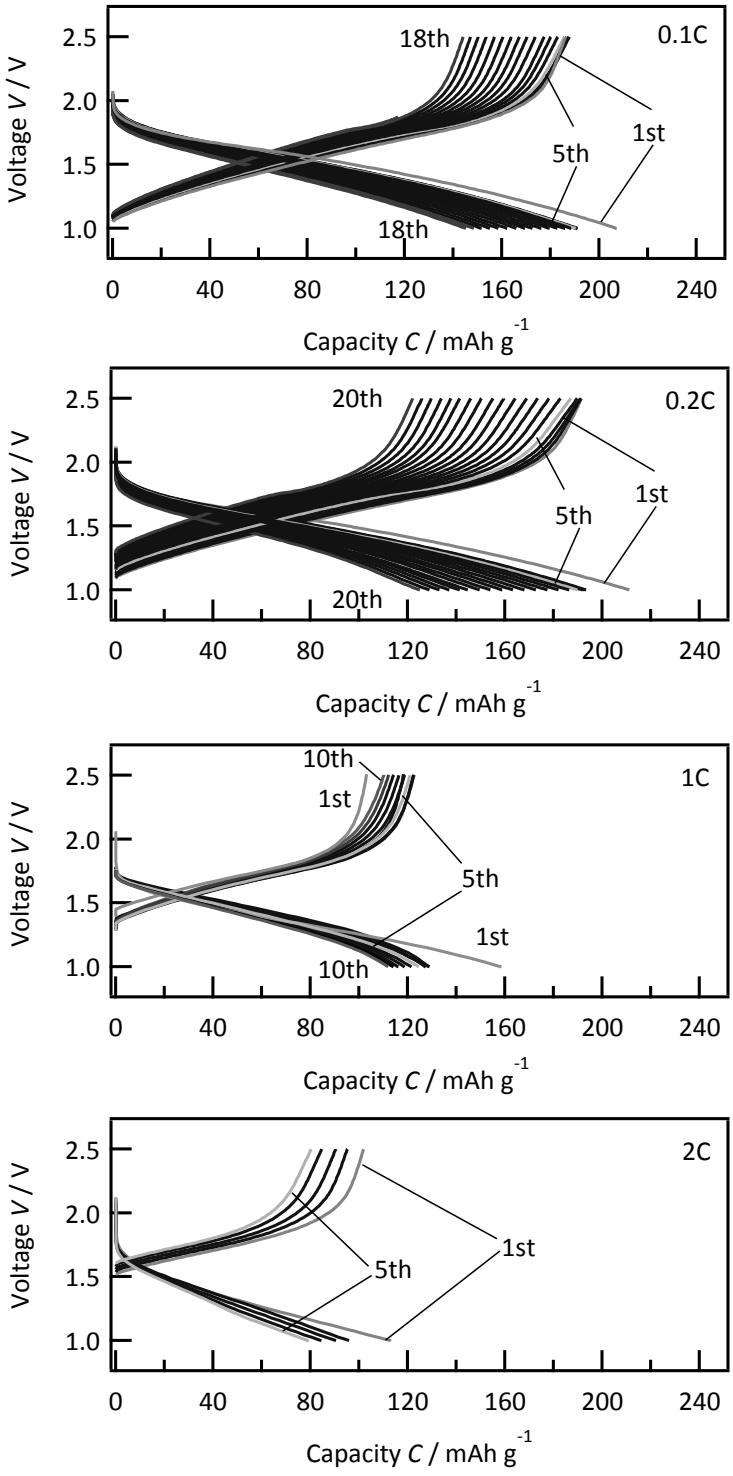

Figure 5. Charge/discharge curves of $TiS_2/Li_{10}GeP_2S_{12}$/In-Li batteries under different current densities of 0.1, 0.2, 1, and 2 C. The batteries were fabricated with a compressive pressure of 19 MPa and sealed into an unpressed cell.

To clarify the influence of the lattice volume change on the cycle stability, a higher pressure of 228 MPa was applied to fabricate the $TiS_2/Li_{10}GeP_2S_{12}$/In-Li batteries. Figure 6a shows the charge-discharge curve of the $TiS_2/Li_{10}GeP_2S_{12}$/In-Li battery, which was compressed at 230 MPa and sealed into an unpressed cell container. At a current density of 1 C, the reversible capacities at the first and second cycles were 160 and 127 mAh g^{-1}, respectively, which are similar values to the battery compressed at 19 MPa (Figure 5c). In contrast, at the tenth cycle, the battery compressed at 230 MPa exhibited the discharge-charge capacities of 120 and 117 mAh g^{-1}, respectively. Increasing the pressure during fabrication improved the cycle stability. Figure 6b shows the charge-discharge curves of a battery compressed at 230 MPa and maintained at the applied pressure during charge-discharge operation. The first discharge-charge capacities were 200 and 145 mAh g^{-1}, respectively. The discharge-charge capacities were improved to 175 and 168 mAh g^{-1}, respectively, at the second cycle and were in the initial ten cycles. This result demonstrates that the cycle stability is considerably improved by increasing the applied pressure. Figure 7 shows the rate capability of a $TiS_2/Li_{10}GeP_2S_{12}$/In-Li cell under an applied pressure of 228 MPa throughout the charge-discharge operation. The current densities used were 0.1, 0.5, 1, 2 and 5 C, and each rate test was performed for three cycles. At 0.1 C, the capacity was 1.7 times higher than that at 1 C. The capacity at 5 C was half of that at 1 C, which is much better than that of a cell under no pressure. After rate testing, the cell was operated again at 0.1 C, and no significant change in the capacity was observed compared to that of the initial cycle at 0.1 C. This result indicates that the cell did not degrade even when operated at high current densities. The applied pressure maintains good contact between the active material and solid electrolyte, resulting in high charge-discharge capacities with high cycle retention.

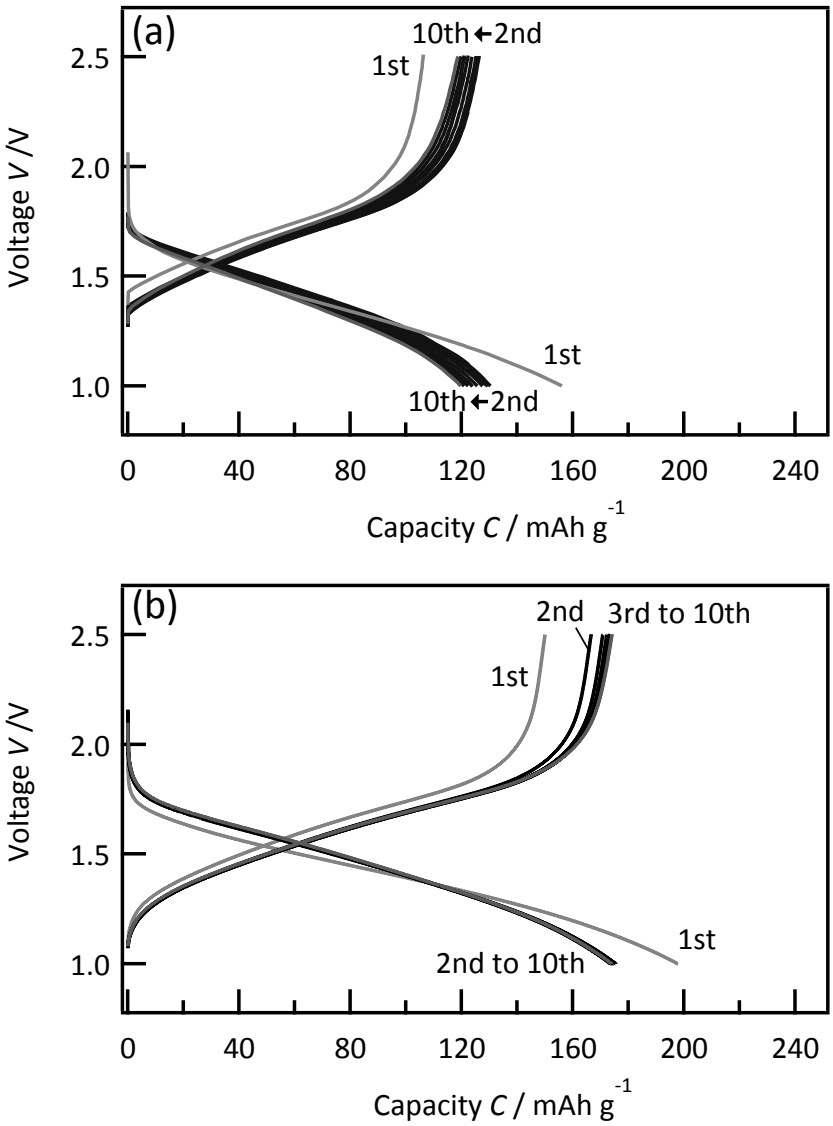

Figure 6. Charge/discharge curves of $TiS_2/Li_{10}GeP_2S_{12}$/In-Li batteries under operation at 1 C. (a) The cell was compressed at 230 MPa and sealed into an unpressed cell. (b) The cell was compressed at 230 MPa, and the pressure was applied throughout the charge/discharge operation.

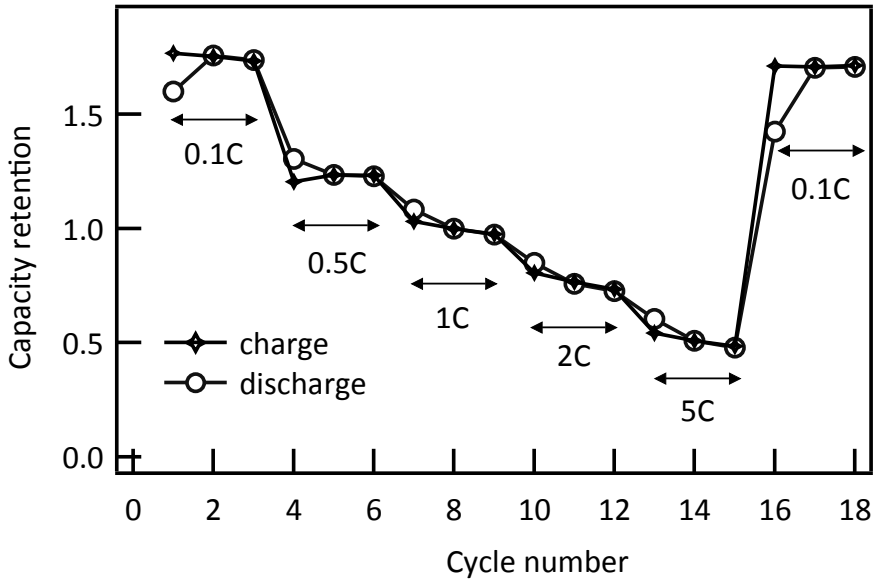

Figure 7. Rate capability of a $TiS_2/Li_{10}GeP_2S_{12}$/In-Li cell with an applied pressure of 230 MPa throughout charge/discharge operation.

Generally, sulfide electrolytes are chemically unstable to moisture in ambient air. Note that the electrochemical tests with applying the pressure of 230 MPa were performed in the Ar-filled glove box. Thus, the inert condition could suppress the degradation of the $Li_{10}GeP_2S_{12}$ electrolyte and lead to the high cycle stability of the battery. To separate the effects of pressure and moisture, the following experiments were performed: (a) a cell was operated with a 230 MPa pressing for 40 cycles in the glove box; (b) a cell was operated with a 230 MPa pressing for 20 cycles and then was operated with no applying pressure for 20 cycles, with all tests performed in the glove-box; (c) a cell was operated with a 230 MPa pressing for 20 cycles in glove box and then was operated with no applying pressure for 20 cycles in air. Figure 8 shows the capacity retention per cycle number for the $TiS_2/Li_{10}GeP_2S_{12}$/In-Li cells operated under the above conditions. The initial capacities are normalized to 1. The cell tested under condition (a) showed the high capacity retention of the discharge capacity from the second to fortieth cycle. Under conditions (b) and (c), the capacities drastically

decreased after the applying pressure was stop at the twentieth cycle. No significant contamination of moisture into the cell was observed under the experimental conditions in this study. These results reveal that the physical contact between the TiS_2 electrode and $Li_{10}GeP_2S_{12}$ electrolyte determines the rate capability and cycle stability of all-solid-state batteries with the TiS_2 cathode.

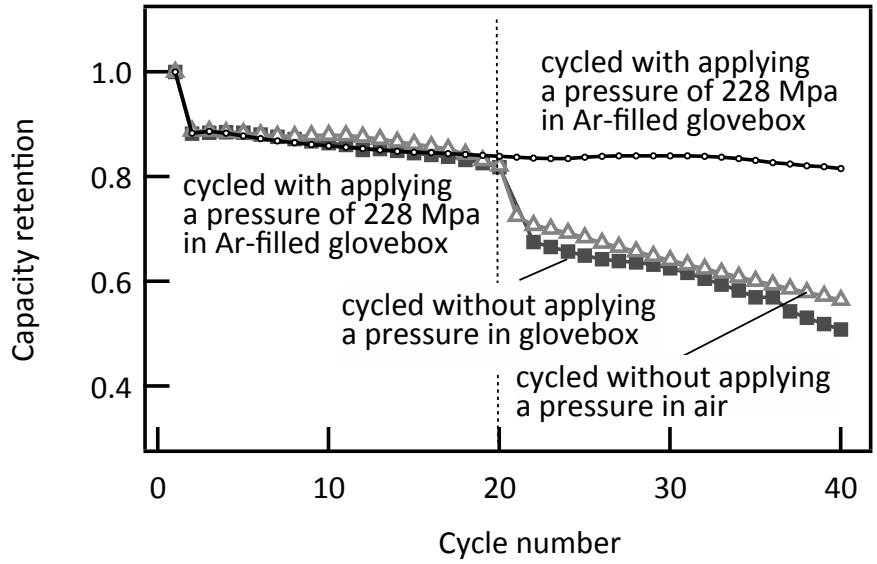

Figure 8. Capacity retention for cycle number of $TiS_2/Li_{10}GeP_2S_{12}$/In-Li cells operated with a 230 MPa pressed cell in glove-box, an unpressed cell in glove-box, and an unpressed cell in ambient air. All cells were operated for initial 20 cycles with applying a pressure of 230 MPa. The current density was 1C.

4.5 Conclusion

All-solid-state batteries were fabricated using a TiS_2 cathode, a $Li_{10}GeP_2S_{12}$ electrolyte, and an In/Li anode, and their electrochemical properties were investigated based on the applied pressure during charge-discharge cycles. The batteries exhibited poor rate capability and severe cycle retention with no applying pressure during the cycles, because the physical contact between the TiS_2 and the $Li_{10}GeP_2S_{12}$ deteriorated by the large volume change of the Li_xTiS_2. The rate capability and severe cycle

retention were greatly improved in the batteries operated with an applying pressure of 230 MPa. Eliminating the volume change of the composite electrodes is important for achieving stable battery operation and performance.

References

[1] T. Kobayashi, Y. Imade, D. Shishihara, K. Homma, M. Nagao, R. Watanabe, T. Yokoi, A. Yamada, R. Kanno, T. Tatsumi, *J. Power Sources*, 182 (2008) 621.

[2] T. Kobayashi, A. Yamada, R. Kanno, *Electrochim. Acta*, 53 (2008) 5045.

[3] T. Inada, T. Kobayashi, N. Sonoyama, A. Yamada, S. Kondo, M. Nagao, R. Kanno, *J. Power Sources*, 194 (2009) 1085.

[4] R. Kanno, M. Murayama, *J. Electrochem. Soc.*, 148 (2001) A742.

[5] F. Mizuno, A. Hayashi, K. Tadanaga, M. Tatsumisago, *Solid-State Lett.*, 8 (2005) A603.

[6] R. Murugan, V. Thangadurai, W. Weppner, *Angew. Chem. Int. Ed.*, 46 (2007) 7778.

[7] N. Kamaya, K. Homma, Y. Yamakawa, M. Hirayama, R. Kanno, M. Yonemura, T. Kamiyama, Y. Kato, S. Hama, K. Kawamoto, A. Mitsui, *Nature Mater.*, 10 (2011) 682.

[8] S. Boulineau, M. Courty, J.-M. Tarascon, V. Viallet, *Solid State Ionic*, 221 (2012) 1.

[9] Y. Kato, K. Kawamoto, R. Kanno, M. Hirayama, *Electrochemistry*, 80 (2012) 749-751.

[10] J. M. Whiteley, J. H. Woo, E. Hu, K. W. Nam, S. H. Lee, *J. Electrochem. Soc.*, 161 (2014) A1812.

[11] H. Meng, B. Huang, J. Yin, X. Yao, X. Xu, *Ionics.*, 21 (2015) 43.

[12] A. Sakuda A. Hayashi, M. Tatsumisago, *Chem. Mater.*, 22 (2010) 949.

[13] N. Ohta, K. Takada, L. Zhang, R. Ma, M. Osada, T. Sasaki, *Adv. Mater.*, 18 (2006) 2226.

[14] N. Ohta, K. Takada, I. Sakaguchi, L. Zhang, R. Ma, K. Fukuda, M. Osada, T. Sasaki, *Electrochem. Commun.*, 9 (2007) 1486.

[15] W. J. Li, M. Hirayama, K. Suzuki, R. Kanno, *Solid State Ionics*, (2015) doi: 10.1016/j .ssi.2015.1005.1007.

[16] J. E. Trevey, C. R. Stoldt, S.-H. Lee, *J. Electrochem. Soc.*, 158 (2011) A1282.

[17] A. Hayashi, T. Matsuyama, A. Sakuda, M. Tatsumisago, *Chem. Lett.*, 41 (2012) 886.

[18] T. A. Yersak, Y. Yan, C. Stoldt, S. H. Lee, *Electro. Letters.*, 1 (2012) A21.

[19] B. R. Shin, Y. J. Nam, D. Y. Oh, D. H. Kim, J. W. Kim, Y. S. Jung, *Electrochim. Acta*, 146 (2014) 395.

[20] S. N. Patel, A. A. Balchin, *Zeitschrift fur Kristallographie.*, 164 (1983) 273.

[21] J. R. Dahn, W. R. McKinnon, R. R. Haering, W. J. L. Buyers, B. M. Powell, *Can. J. Phys.*, 58 (1980) 207.

[22] M. S. Whittingham, *Science*, 192 (1976) 1126.

[23] Y. Mo, S. P. Ong, G. Ceder, *Chem. Mater.*, 24 (2012) 15.

[24] S. P. Ong, Y. Mo, W. D. Richards, L. Miara, H. S. Lee, G. Ceder, *Energy Environ. Sci.*, 6 (2013) 148.

[25] Y. Takahashi, N. Kijima, K. Dokko, M. Nishizawa, I. Uchida, J. Akimoto, *J. Solid State Chem.*, 180 (2007) 313.

Chapter 5

Summary

Energy density is a key issue to be addressed for the development of all solid-state batteries. Poor lithium conductivity in solid electrolytes and at solid/solid interfaces in electrode/electrolyte composites limit the current drain in all solid-state batteries. Recent research on solid electrolytes have found an extremely high ion conductive material LGPS as compared with liquid organic electrodes. However, there is very little information available for the solid/solid interfaces of the LGPS and electrode materials. In this thesis, two composite cathodes $LiNbO_3$-$LiCoO_2$/LGPS and TiS_2/LGPS were fabricated as cathodes in all solid-state batteries. Various fabrication conditions such as mixing methods, particle sizes, and surface coating on electrodes were investigated to develop composite electrodes with high capacity, high current density, and high stability. The results are summarized as follows.

In chapter 3, $LiNbO_3$-coated $LiCoO_2$/LGPS composites have been fabricated, and electrochemical reactions of $LiCoO_2$/LGPS/In-Li have been clarified. The key parameters associated with the improvement of the reaction efficiency are summarized as follows.

(1) The LGPS particles readily aggregate during the mixing process. Highly dispersed composites can be successfully obtained under mild grinding.

(2) Surface coating of $LiNbO_3$ on $LiCoO_2$ is effective to decrease the reaction resistance at the $LiCoO_2$/LGPS interface. The weight ratio of $LiNbO_3$ to $LiCoO_2$ should be over 0.5 wt.%.

(3) The $LiCoO_2$/LGPS composite fabricated with the optimized condition exhibits the

first discharge capacity of 124 mAh g^{-1} which is comparable to that observed in lithium-ion batteries

(4) The $LiNbO_3$/$LiCoO_2$/LGPS/In-Li cell shows capacity fading caused by the increase in the resistance to lithium diffusion at the In-Li/LGPS interface.

In Chapter 4, TiS_2/LGPS composites have been fabricated, and their electrochemical properties have been clarified as follows.

(1) Nanosized TiS_2 particles lead to highly dispersed composites with LGPS.

(2) Fast lithium diffusion occurs at the TiS_2/LGPS interface. However, the large volume changes during the lithium intercalation decreases the physical contact among TiS_2 particles and between TiS_2 and LGPS particles, which leads to severe capacity retention during the cycling.

(3) The rate capability and severe cycle retention can be remarkably improved in the batteries operated with an applying pressure. Eliminating the volume change of the composite electrodes is important for achieving stable battery operation and performance.

Both $LiCoO_2$/LGPS and TiS_2/LGPS composites exhibit reversible charge-discharge reactions under high current density when the optimized conditions are used for the fabrication. These results indicate that the LGPS-type materials are one of the most promising candidates as the solid-electrolyte in the composite electrolytes. However, a highly-resistive interface is formed between the bare $LiCoO_2$ and the LGPS. The surface coating of $LiNbO_3$ is needed to decrease the interfacial resistance. In contrast, the TiS_2/LGPS composite delivers high rate capability without modification of the TiS_2 surface. It is indicative of that the sulfide/sulfide interface is suitable for fast lithium diffusion. In contrast, the large volume change of TiS_2 during lithium intercalation leads to severe capacity fading. From the above results, the research directions for the future can be concluded as follows. For oxide materials for composite cathodes with the

LGPS-type electrolytes, the development of coating materials is crucial to achieve high current drain of the cathodes in all solid-state batteries. For sulfide materials for composite cathodes, key issues to be addressed are 1) materials research of new sulfide that shows a small volume change during lithium intercalation and 2) development of casting structures that eliminates the volume change of composite electrodes. The groundbreakings regarding to these issues will play an active role in the development of all solid-state batteries for practical use.

Acknowledgement

The author would like to express greatly gratitude to Professor Ryoji Kanno of the Tokyo Institute of Technology for his warm encouragements and thoughtful discussion on this thesis.

The author would like to express greatly gratitude to Vice Professor Masaaki Hirayama of the Tokyo Institute of Technology for his continuous patient guidance and valuable discussion on my research during whole doctor course.

The author wishes to thank all the members of Kanno-Hirayama laboratory for continuous encouragements and helpful discussions.

The author would like to express appreciate a Grant-in-Aid from the Advanced Low Carbon Technology Research and Development Program, Specially Promoted Research for Innovative Next Generation Batteries (ALCA- SPRING) of the Japan Science and Technology Agency (JST), for supporting the research.

The author also would like to express gratitude to Japan and Grand-in-Aid for Scientific Research of Ministry of Education, Culture, Sports, Science and Technology, Japan (MEXT Grant), for the scholarship supporting of doctor course.

Finally, the author would like to express his sincere gratitude to his parents for their supporting, understanding, and encouragement.

January 2016

Li Wenjing